Variability of bottom carbonate chemistry over the deep coral reefs in the Florida Straits and the impacts of mesoscale processes

Mingshun Jiang[1*], Chudong Pan[1,#], Leticia Barbero[2], John Reed[1], Joe Salisbury[3], James H. VanZwieten[4], and Rik Wanninkhof[2]

[1]Harbor Branch Oceanographic Institute, Florida Atlantic University

[2]Atlantic Oceanographic and Meteorological Laboratory, NOAA

[3]Ocean Process and Analysis Laboratory, University of New Hampshire

[4]Department of Civil, Environmental and Geomatics Engineering, Florida Atlantic University

Submitted to Ocean Modeling

June 5, 2019

October 24, 2019, 1st revision

December 10, 2019, 2nd revision

*Corresponding author: jiangm@fau.edu, Telephone: 1-772-242-2254.
#Current address: NOAA, National Ocean Service, Silver Spring, MD 20910.

Abstract

Abundant and diverse cold-water coral and fish communities can be found in the deep waters of the Florida Straits, which are believed to be living under suboptimal conditions impacted by increasing oceanic CO_2 levels. Yet, little is known regarding the spatial-temporal variability of bottom carbonate chemistry parameters and their dynamic drivers in this area. To address this issue, we present results from numerical simulations of a coupled physical-biogeochemical model for the south Florida shelf and Florida Straits. Our exploratory analysis focuses on two well-known deep-coral habitats: Pourtalès Terrace (200-450 m) and Miami Terrace (270-600 m). Results suggest that bottom waters along the northern/western slope of the Straits are comprised primarily of the North Atlantic Central Water (NWCW) and Antarctic Intermediate Water (AAIW), driven by upwelling associated with the bottom Ekman transport of the Florida Current. Over the Pourtalès Terrace, both the meandering of the Florida Current and mesoscale eddies modulate the upwelling (downwelling) of cold (warm) waters. In contrast, Florida Current makes a sharp turn at the southern end of the Miami Terrace leading to persistent island wakes, frequent occurrences of a transient eddy, and strong upwelling of deep waters toward the platform of the terrace. Passage of the transient eddy often accompanies strong downwelling of warm waters and a return (southward) flow on top of the platform. Overall, bottom water properties including temperature (T), dissolved inorganic carbon (DIC) and total alkalinity (TA) show strong variability on weekly to monthly time-scales over entire Pourtalès Terrace and on the platform of Miami Terrace mostly driven by physics. In deeper areas (>400 m), bottom water properties are fairly stable with both DIC and TA showing narrow ranges. Interestingly, waters over the southeastern portion of the Pourtalès Terrace show consistently warmer temperature, lower DIC, and higher TA than those on top of this terrace. The aragonite

saturation state (Ω) ranges 1.2-2 on top of the Pourtalès Terrace and 1.2-1.7 both on top of Miami Terrace and on the upper slope of Pourtalès Terrace. In the deeper slope areas (> 400 m), it is nearly constant at 1.2-1.3. This modeling effort suggests that remote forcing and biogeochemical processes along the transport paths, from the Gulf of Mexico to the Straits, are significant but second-order contributors to the variability of bottom carbonate chemistry. The impacts of benthic biogeochemical processes along the transit paths are not resolved.

Key words: Coupled physical-biogeochemical model, mesoscale eddies, upwelling, aragonite saturation state, deep corals, Florida Straits.

53 **1. Introduction**

54 In the North Atlantic Ocean, deep-sea coral ecosystems (DSCEs) are found most
55 extensively off the coasts of Europe (Roberts, 2009 and reference therein) and the southeastern
56 United States (SEUS), from North Carolina to Florida (Ross and Nizinski, 2007; Reed et al. 2005,
57 2006, 2013) (Figure 1). Off eastern Florida alone, it is estimated that deep-water coral habitats
58 may extend over 13,440 km^2 (Reed et al. 2013). These DSCEs support diverse and abundant
59 invertebrate and fish communities (Reed et al. 2005, 2006; Ross and Quattrini, 2007), and have
60 been increasingly appreciated over the past decades as their extensive footprint is better
61 understood. For example, the deep-water *Oculina* coral reefs off the east coast of Florida were
62 the first deep-water Coral Habitat Areas of Particular Concern (CHAPC) in the world, designated
63 by the National Oceanic Atmospheric Administration (NOAA) in 1984. Recently, NOAA
64 designated five new deep-water CHAPCs in the SEUS, covering 62,714 km^2 (NOAA, 2010).
65 The majority of these DSCEs occur within continental shelves and slopes, which are expected to
66 experience the greatest changes in environmental stressors (e.g. temperature, pH) due to climate
67 change, ocean acidification, and deoxygenation on top of the large natural variability as
68 compared to other portions of the deep-sea (e.g. Mora et al. 2013; Lunden et al. 2014; Perez et al.
69 2018).

70 It has been widely recognized that warming water temperatures and increasing CO_2 pose
71 serious threats to the health of shallow coral reefs (e.g. Bellwood et al. 2004; Kleypas and Yates,
72 2009; Anthony et al. 2011). Less attention has been paid to deep-water reefs that are already
73 living under high CO_2 conditions. The potential impacts of ocean acidification on deep corals
74 and the deep coral ecosystems remains poorly understood (e.g. Hoegh-Guldberg et al. 2017).
75 Limited experimental studies focused mainly on the growth and calcification rates of reef-

76 building *Lophelia pertusa* and these results are mixed (e.g. Thresher et al. 2011; Maier et al.
77 2009, 2012; Lunden et al. 2014; Georgian et al. 2016a; Buscher et al. 2017; Gomez et al. 2018).
78 The potential impacts may also include metabolism, reproduction capability, and the dissolution
79 of coral reefs structures. Thus, it is important to better characterize the current mean state and
80 variability of bottom carbonate chemistry over deep-water reefs. Significant progress has been
81 made in observing environmental conditions of DSCEs including hydrodynamic and
82 biogeochemical conditions (e.g. Mienis et al. 2012, 2014; Lunden et al. 2013; Ross et al. 2015;
83 Georgian et al. 2016b). Yet information about carbonate chemistry conditions over the DSCEs
84 remains scarce. This limits our capability to properly understand the potential threat of rising
85 oceanic CO_2 to these communities. Limited studies suggest that the aragonite saturation state
86 (Ω_{Ar}) is only marginally higher than 1.0 over the shelf slope in the Gulf of Mexico (GOM) and
87 the Straits of Florida regions (Lunden et al. 2013; Wang et al. 2013; Wanninkhof et al. 2015).
88 The three Gulf of Mexico and East Coast Carbon Cruises (GOMECC-1, 2 & 3) conducted in
89 July 2007, 2012 and 2017, respectively, surveyed the same transect (27^{o}N) in the northern
90 Florida Straits yielding very similar Ω_{Ar} measurements, with values near the sea floor being only
91 slightly higher than 1. For example, the minimum Ω_{Ar} was 1.19 and 1.36, respectively, for the
92 west and east Florida slope during GOMECC2. Thus, progressive ocean acidification poses a
93 significant threat to deep coral reefs by further lowering pH and reducing the availability of
94 carbonate ions (CO_3^{2-}), particularly for aragonite, which is incorporated into scleractinian
95 skeletons (Cohen and Holcomb, 2009; Perez et al. 2018).
96 Deep reef systems in this region are subjected to strong physical disturbances including
97 upwelling, eddy entrainment and mixing, and the meandering of the Florida Current (FC). In the
98 Straits of Florida the FC is the dominant current, with speeds that can exceed 2 m s^{-1}. This

current originates from the Loop Current (LC) in the GOM and feeds into the Gulf Stream in the South Atlantic Bight. The FC impinges on the shelf of the Florida Keys and its core is mainly situated over the northwestern slope of the Straits, with persistent upwelling driven by the current-induced bottom Ekman transport (e.g. Pietrafesa, 1990; Garrett et al. 1993). The FC also exhibits mesoscale meanders with periods of 5 and 12 days and with wavelengths of, respectiveloy, 170 and 340 km (Johns and Schott, 1987), which can substantially vary the bottom temperature, salinity and velocities over these timescales. The FC also generates mesoscale (30-100 km) cyclonic eddies and sub-mesoscale (10-30 km) features along the shelf break (e.g. Lee, 1975; Lee and Mayer, 1977; Lee et al. 1995; Fratantoni et al. 1998). These dynamic features can further drive strong upwelling of CO_2-rich cold waters up the slope and onto the shelf (e.g. Smith, 1981; Pitts and Smith, 1997; Kourafalou and Kang, 2012; Xu et al. 2012), exposing the shelf fauna to cold, low pH, deep ocean waters.

In this manuscript we examine the temporal variability of key carbonate parameters including total dissolved inorganic carbon (DIC), total alkalinity (TA), pH, and Ω_{Ar}, in the deep waters of the Florida Straits using a newly developed coupled physical-biogeochemical model and *in situ* measurements from shipboard surveys and bottom moorings. We focus on two key coral habitats, the Pourtalès Terrace and Miami Terrace (e.g., Reed et al. 2013, 2014). The Pourtalès Terrace lies in the southern slope of the Florida Keys, at depths between 200-450 m and a maximum width of 32 km. This 213 km long terrace consists of extensive, high relief, hard bottom, and essential fish habitats covering 3,429 km^2 (Figure 1). The southeastern flank of this terrace (between 81°12´-80°24´W) is located in the lee of Florida Current and is a CHAPC. Benthic communities on this terrace are dominated by stylasterid hydrocorals, gorgonian alcyonaceans, black corals, and sponges; the scleractinian corals include *Lophelia pertusa,*

122 *Enallopsammia profunda, Madracis myriaster, Madrepora oculata, Solenosmilia variabilis*, and
123 *Dendrophylliidae* and one *L. pertusa* mound was recently discovered on the Terrace slope (Reed
124 et al. 2005, 2014). The fish communities consist of 62 species, including eleven commercially
125 and recreationally important fish species (Reed et al. 2014). To the north of the Pourtalès Terrace
126 is the Miami Terrace (25°18'-26°30'N), which extends 145 km long at depths from 275 to 600 m.
127 The terrace covers 2,329 km^2 and has similar benthic biota as Pourtalès Terrace and
128 *Lophelia/Enallopsammia* coral mounds and coral rubble are common at the foot of the
129 escarpment (Reed et al. 2006; Vinick et al. 2012).
130 The objectives of this manuscript are two-fold: 1) further assessment of model skills in
131 simulating the deep water upwelling, mesoscale eddies, and near bottom water properties in the
132 Florida Straits, and 2) characterization of spatial-temporal variability of bottom water properties
133 especially carbonate chemistry and controlling processes including mesoscale eddies and current
134 meandering. The numerical model and *in situ* data used for assessing model skills are described
135 in Section 2. Model results including a comparison with *in situ* data, key physical and carbonate
136 chemistry features, and the variability of near bottom water properties are presented in Section 3.
137 In Section 4, key controlling processes for this variability are discussed, including meso- and
138 submesoscale eddies and associated upwelling, large-scale transport and mixing, and
139 biogeochemical processes such as local export and remineralization of organic carbon. Finally,
140 some concluding remarks are made in Section 5.
141
142 **2. Methods**
143 **2.1. Model**
144 The numerical model is based on the Regional Ocean Modeling System (ROMS), a three-

145 dimensional primitive equation ocean model system (e.g. Shchepetkin and McWilliams, 2005).
146 The model domain covers the south Florida shelf, Florida Straits, northern Cuban coastal region
147 and western Great Bahamas Bank, with a horizontal resolution ~ 1.5 km and 35 sigma layers
148 vertically concentrating near the surface (Figure 1). The numerical schemes for momentum
149 equations and tracers are third-order upstream for horizontal advection, and fourth-order centered
150 difference for vertical advection. Vertical turbulent mixing is computed with the generic length
151 scale (GLS) turbulent closure (Umlauf and Burchard, 2003). A uniform horizontal and viscosity
152 and mixing coefficient of 10 m^2/sec were applied on the geopotential surfaces (Haidvogel and
153 Beckmann, 1999). The model is driven by surface meteorological forcing derived from the 3-
154 hourly North American Regional Reanalysis (NARR, Mesinger et al. 2006), open boundary
155 forcing derived from the 1/25^o Gulf of Mexico Hybrid Coordinate Ocean Model (HYCOM,
156 Chassignet et al. 2009) output, and the local run-off collected at the USGS gauges
157 (http://waterdata.usgs.gov/nwis). Results presented in this manuscript are from a run without
158 tidal forcing. Tides are important over the south Florida shelf and shelfbreak (e.g. Leichter et al.
159 2007) but tidal currents are moderate, ~20 cm/sec, over the mid to lower slope. Temperature
160 anomalies at tidal frequencies are small with the standard deviations at 0.16^{o}C and 0.09^{o}C,
161 respectively, as observed at the T2 and T3 stations. In order to avoid drift of sea surface
162 temperature (SST) on the continental shelf, particularly shallow areas, model SST is relaxed to
163 observed daily SST from satellite observed SST (http://podaac.jpl.nasa.gov/). The modeled
164 period was chosen as 2011-2012. More details for the physical model can be found in Pan et al.
165 (2017). Unlike the previous simulations reported in Pan et al. (2017), the model bathymetry cut-
166 off is now 2000 m instead of 1500 m.
167 The physical model is coupled with a biogeochemical model developed by Fennel et al.

(2006, 2008), with some modifications made to parameter values (see Table 1). This model has 6 functional groups that describe the nitrogen cycle through the lower food web, nitrate (NO_3) and ammonia (NH_4), phytoplankton, zooplankton, small detritus and large detritus. Chlorophyll is a diagnostic variable based on the phytoplankton chlorophyll to carbon ratio, which is computed following the light acclimation model by Geider et al. (1998). It also includes DIC, dissolved oxygen (DO), and TA. In our implementation, we adjusted some key parameters such as light attenuation and half saturation constants (Table 1) in order to better simulate deep ocean phytoplankton dynamics, including the reproduction of the deep chlorophyll maximum. The simulation of the carbon cycle largely follows the nitrogen cycle, with a fixed Redfield carbon to nitrogen ratio of 6.625. The air-sea CO_2 flux is determined by the air-sea partial pressure of CO_2 (pCO_2) multiplied by the gas-transfer (or piston) velocity, which is computed following the formulation of Wanninkhof (1992). Alkalinity is assumed to be unaffected by air-sea gas exchange of CO_2, but instead altered by a number of biogeochemical processes, including calcite formation and dissolution, nitrate uptake and regeneration, and sulfate reduction. In this model, only the nitrate uptake and remineralization of organic nitrogen are included. Based on the model output, pH and Ω_{Ar} were computed from DIC and TA using a Matlab co2sys package with K1 and K2 constants from Mehrback et al. (1973) and K_{SO4} from Dickson (1990) (see Lewis and Wallace, 1998; Van Heuven et al. 2011).

The biogeochemical parameters in the river inputs to the model include nutrients (NO_3, NH_4), dissolved organic matter, DIC and TA. There are only very limited measurements for biogeochemical parameters in the rivers. For simplicity, in this simulation we used constant values (5 µmol/l for NO_3, 4 µmol/l for NH_4, 120 µmol/kg for DOC, 2100 µmol/kg for DIC and 2300 µmol/kg for TA) based on the available data compiled by the South Florida Water

191 Management District (http://my.sfwmd.gov/dbhydroplsql/show_dbkey_info.main_menu). This
192 choice will affect the biogeochemical results including nutrients, phytoplankton biomass, DIC
193 and TA in nearshore and coastal areas, but we do not expect it to significantly affect water
194 properties in the offshore areas particularly bottom waters in the Florida Straits, where river
195 influences are minimal. Construction of more detailed river inputs is currently underway.
196 The boundary conditions for nitrate, DIC and TA were prescribed based on their
197 respective nonlinear regressions with temperature derived from observed concentrations along
198 the west Florida Slope transect during GOMECC2 cruise (Figure 2). The boundary temperature
199 field was derived from GOMex model output as described above. The assumption is that these
200 water properties along the western boundary are generally similar because all waters in the GOM
201 come from the subtropical North Atlantic through the Caribbean Sea (Rivas et al. 2005). Local
202 physical-biogeochemical processes will undoubtedly modify the water properties. There is
203 insufficient information to specify more detail (e.g. spatial gradients) along the boundary. The
204 NO_3, DIC and TA concentrations are all strong correlated with both the temperature and salinity
205 as observed along the western Florida shelf slope during GOMECC2 cruise (Figure S1). Yet,
206 both the NO_3 and DIC correlations with temperature (r=0.99 NO_3 and r=0.98 for DIC) for were
207 much stronger than those with salinity (r=0.93 for NO_3 and r=0.9 for DIC), while the TA
208 correlation with temperature was similar with that with salinity. Therefore, temperature was used
209 to construct the model boundary conditions for the NO_3, DIC, and TA.
210 The boundary conditions for other biogeochemical variables are derived from the output
211 of the coupled ROMS-CoSINE (Carbon, Silicon, Nitrogen Ecosystem) model developed by Dr.
212 Chai at the University of Maine (Chai, *pers. comm.*). The CoSINE model was originally
213 developed for the Pacific Ocean, but was adapted for the northwest Atlantic Ocean (Xiu and

214 Chai, 2014). The model consists of 31 state variables describing 3 types of nutrients (N, P, Si), 3
215 phytoplankton functional groups (picoplankton, diatoms, and coccolithophorids), 2 size classes
216 of zooplankton (microzooplankton, mesozooplankton), bacteria, several groups of organic matter,
217 dissolved oxygen (DO), total alkalinity, and TCO_2. The model was coupled with a 7-km ROMS
218 model with a domain covering the Northwest Atlantic region including the Gulf of Mexico. A
219 50-yr (1957-2007) simulation of the coupled model has been performed, and the physical model
220 has been calibrated, indicating satisfactory model skills including capturing the Gulf Stream
221 dynamics (Kang and Curchitser, 2013). No systematic calibration or validation, however, has yet
222 been made for the biogeochemical simulation. We used the biogeochemical results from the last
223 two years (2006-2007), an arbitrary choice, to derive biogeochemical boundary conditions for
224 our modeling period (2011-2012) because the ROMS-CoSINE simulation for this period is not
225 available. We do not, however, expect this temporal miss-match to significantly impact model
226 calculations as the three key parameters (nitrate, DIC and TA) were specified separately from the
227 CoSINE results. At present, we have no sufficient observed data for specifying other biological
228 variables (PON/POC, DON/DOC, plankton biomass) in the Gulf of Mexico. The justification of
229 our choices for these boundary parameters is provided in the Supplement Materials, which
230 include a figure showing the temporal variability of key biogeochemical variables along the
231 western boundary on the west Florida Slope (Figure S3). The time mismatch in boundary
232 conditions and lack of validation of the biological parameters means that the results should be
233 viewed with a degree of uncertainty, due to the previously mentioned factors. As much of the
234 carbon dynamics are driven by well-constrained physical variability in the domain the processes
235 and patterns are representative of actual conditions.
236

237 **2.2. Data**

238 Extensive model calibration has been performed for the physical model using available
239 data from various sources (Pan et al. 2017). In this manuscript we compare model results with
240 data collected in the Florida Straits from four sources, which have not been used in the
241 calibration by Pan et al. (2017): 1) integrated transport between west Palm Beach and Grand
242 Bahamas Island (between 26-27ºN) through the northern Florida Straits (Meinen et al. 2010); 2)
243 the second Florida Shelf-Edge Experiment (FloSEE) cruise, which took place in September 11-
244 November 10, 2011; 3) the GOMECC2 cruise, which took place in July-August, 2012; and 4)
245 near bottom temperature and current profiles measured by Acoustic Doppler Current Profilers
246 (ADCPs) at two mooring stations on the Miami Terrace (Figure 1). We also compare the model
247 output of biogeochemical variables with limited data collected during the FloSEE and
248 GOMECC2 cruises.

249 The transport by Florida Current through the northern Florida Straits has been measured
250 using various methods at around 27°N. Here, we use the estimates based on the voltage change
251 to a submarine telephone cable due to the current-induced changes in magnetic field, which
252 covered various periods from1970 to present (Meinen et al. 2010). The transport was calibrated
253 with the more accurate estimates based on the time lapse of a free falling dropsonde at a series of
254 stations across the Straits that took place about once per month (Niiler and Richardson, 1973;
255 Garcia et al. 2014). Tidal signals were removed from the final transport estimate.

256 The FloSEE cruise, onboard the NOAA ship *Nancy Foster*, focused on the Pulley Ridge
257 mesophotic coral reef ecosystem on the southwest Florida shelf, with the objective of studying
258 the potential impacts of the Deepwater Horizon oil spill event on south Florida coral reefs (Reed
259 et al. 2012). In addition to benthic surveys (e.g. coral species, video of benthic habitats, images

from side-scan sonars) with a Remotely Operated Vehicle (ROV), a Bluefin spray glider was deployed for measuring water properties (T, S) over the outer shelf of the southwest Florida shelf (see Pan et al. 2017). Traditional CTD casts were also made over Pulley Ridge, the Pourtalès Terrace (4 stations) and southern slope off Key West (1 station) (Figure 1). Water properties measured using a Sea-Bird 911plus CTD rosette system included temperature, salinity, turbidity, fluorescence, pH, and dissolve oxygen (DO). Collected data were binned into 1 m depth intervals. For this manuscript, we only used the data from the CTD stations over the Pourtalès Terrace.

The GOMECC cruises were funded by NOAA's Ocean Acidification Program (OAP), with cruises conducted in summers of 2007, 2012, and 2017 to measure hydrological and carbonate chemistry parameters in the Gulf of Mexico and U.S. East Coast (only first two cruises) (Wang et al. 2013; Wanninkhof et al. 2015). These cruises covered the GOM and US East Coast, with 18 transects that ran from the coast to deep oceans. Two other NOAA-sponsored cruises, East Coast Ocean Acidification (ECOA) I and II were conducted in 2015 and 2018, respectively, which occupied most of the GOMECC stations on the east coast, but with more detailed surveys in some selected coastal areas. During all of these cruises, a number of physical-biogeochemical parameters were measured with bottled samples including temperature (T), salinity (S), chlorophyll (Chl), macro-nutrients, DIC, TA, and DO, among others. The analysis for chlorophyll samples was limited to the upper 250 m. Results from the first and second GOMECC cruises can be found in Wang et al. (2013) and Wanninkhof et al. (2015), respectively. Yang et al. (2015) examined the variability of total alkalinity in the northeastern Gulf of Mexico using the GOMECC2 data and other historical measurements. Here we will use the data from the bottle samples collected between July 22 – August 13, 2012 during GOMECC2 along two transects that are located inside our model domain: transect 1 extending from Tampa

283 Bay to the shelf break (hereafter referred to as WFL), and transect 2 across the northern Florida
284 Straits (hereafter referred to as EFL) along the Ft. Pierce, FL segment at 27°N (Figure 1). These
285 data indicate strong nonlinear correlations between temperature, DIC, TA and NO_3 especially
286 below the thermocline (Figure 2). In order to corroborate bottom water masses, we also use a
287 portion of the data along A22 transect (~70°-65°W) of the WOCE survey, which took place in
288 March 24-April 17, 2012 (http://whp-atlas.ucsd.edu/atlantic_index.htm). Data used below were
289 from stations 66-81 between 12°36-16°19.7'N, which were within the Caribbean Current that
290 feeds into the Gulf of Mexico.
291 To further evaluate the model predictions, particularly on the temporal dimension, we
292 compare model output with observed time series of near-bottom (~12 meters above the sea floor)
293 temperatures and current profiles. Between 2009 and 2015, ADCP moorings have been
294 periodically deployed on the northern Miami Terrace (latitude ~ 26°4′ N) at 4 locations from 260
295 m to 640 m (Figure 1). Two temperature time-series collected from moorings T2/B2 (320 m total
296 water depth) and T3/B3 (290 m total water depth), and one water velocity time-series measured
297 from mooring T2/B2 (measurement depth of 156 m) are utilized in this study. It is noted that the
298 temperature sensor elevation above the sea floor (~ 12 m) is similar to the water depth of the first
299 model layer from the bottom. For more details about these instruments and measurements please
300 see Machado et al. (2016).
301
302 **3. Results**
303 **3.1. Model skills**
304 Extensive calibration of the physical model has been conducted using the following four
305 data sets (Pan et al. 2017): 1) FloSEE ship deployed CTD data, 2) CTD measurements onboard a

306 Spray glider during two month-long surveys over western Florida Shelf, 3) satellite altimetry
307 measured sea surface height (SSH), and 4) satellite infrared imaged sea surface temperature
308 (SST). Results indicate that the model is able to reproduce the spatial-temporal variability of
309 water properties, as well as key dynamic processes including LC/FC dynamics, formation and
310 propagation of mesoscale eddies associate with the current instability, interactions between
311 eddies and the shelf/slope, and upwelling associated with the eddies and LC/FC meandering (e.g.
312 Johns and Schott, 1987; Kourafaou and Kang, 2012). This previous comparison, however,
313 focuses on the west Florida shelf, particularly in the Pulley Ridge area. Here we provide an
314 additional assessment on the model skills, with a focus on the Florida Straits (Figures 2-6). The
315 relevant statistics of these model-data comparisons are shown in Table 2, where the last column
316 shows the mean model-data differences along with the confidence interval based on the paired
317 student-*t* test.

318 We first present the comparison between model and observed transport at 27^{o}N (Figure
319 3). The result indicates that the model captures the magnitude of volume transport along this
320 section with mean transport at 30.3 vs 31.2 m^3/sec, both are close to recent estimates of the mean
321 transport. However, for unclear reasons, the model under-estimates the variability of volume
322 transport on a monthly timescale (Figure 3a). Modeled variability of volume transport on shorter
323 timescales (<11 day) due to meso- and submesoscale activities is similar to measured data, with
324 standard deviation (std) at 0.8 m^3/sec for model vs 1.1 m^3/sec for data (Figure 3b). Model
325 volume transport also has a weak correlation with measured data, with the correlation coefficient
326 r=0.19 (p<0.05) and r=0.27 (p<0.01), respectively, for the low frequency (>11 day) and high
327 frequency (<11 day) components.

328 A comparison of model and observed key parameters from July 30-31, 2012 along the

329 GOMECC-2 EFL transect is shown in Figure 4. Both modeled results and observations indicate
330 strong bottom upwelling of cold and relatively low salinity waters along the western slope (left
331 side of the current looking downstream) of the transect, as shown in the upward tilting of the
332 isotherms and isopleths of other water properties. This is consistent with the well-known feature
333 of the Florida Current that its main axis is located mid-slope on the west side of the Straits (e.g.
334 Seim et al. 1999). The modeled upwelling in this instance, however, is weaker than the
335 observations, with the modeled temperature of the upper slope water about ~3^{o}C warmer than the
336 measurements (Figure 4a and b). Upwelling was unusually strong during the GOMECC-2 cruise
337 (Zhang et al. 2017). On average, however, model temperature along this transect is only about
338 0.3^{o}C lower than the observed, which is not statistically significant (Table 2). The model is also
339 able to reproduce the general pattern of salinity including the high salinity subsurface layer
340 between 50 – 300 m along the central-right flank of the Florida Current, which represents the
341 North Atlantic salinity maximum waters (SMW) from the subtropical North Atlantic Ocean (see.
342 e.g., Roson et al. 2003). Modeled salinity over the upper western slope is higher than the
343 observed salinity by about 0.25 psu, but the average modeled salinity along this transect agrees
344 well with observations. Both model temperature and salinity show a strong point-to-point
345 correlation with data (r=0.93 and 0.65, respectively) (Table 2).
346 A comparison between model and observed key biogeochemical parameters (DIC, nitrate
347 and TA) along the same transect tells a similar story (Figure 4e-j). The model reproduces the
348 general patterns and ranges of these parameters. However, over the upper slope modeled NO_3
349 and DIC concentrations are lower than the observed (Zhang et al. 2017), whereas modeled
350 alkalinity is about 10-20 μmol/kg higher than the observed (Figure 4i-j) in accord with higher
351 observed upwelling. The point-to-point correlation coefficients and root-mean-square error

(RMSE) between the model and observed values are, respectively, 0.9 and 4.5 μmol/kg for nitrate, 0.96 and 20.4 μmol/kg for DIC, and 0.69 and 18.4 μmol/kg for TA (Table 2). On average, modeled DIC is 8 μmol/kg higher than the observed and modeled TA is 10 μmol/kg higher than the observed. The GOMECC measurement errors for DIC and TA are, respectively, 2 μmol/kg and 4 μmol/kg. Therefore we believe these mismatches are mostly due to model biases. Only a subset of water samples was analyzed for chlorophyll concentration. Along this transect, the data also clearly shows a subsurface maximum with increasing depth at around 30 m at the shelf edge to 100 m offshore, generally in agreement with the model vertical distribution. The overall a point-to-point correlation between model and data is r=0.37 (p<0.01) and r=0.74 after excluding a few outlier (see Figure S2).

The temporal variability of model temperature and current fields are compared with data collected from two ADCP moorings, T2 and T3 (Figure 5). Overall, the model reproduces near-bottom temporal patterns (e.g. dominant periods) reasonably well over weekly-to-monthly timescales. A simple spectral analysis indicates that the model and observed bottom temperatures at T2 and T3 have very similar power spectra with no obvious peak at low frequency (>11 day) but prominent peaks at the 7-day period for high frequency variability (<11 days) (not shown). Modeled and observed temperatures at both locations have similar magnitudes in high frequency variability (Figure 5a, b). The model and observed stds are 0.52 and 0.67 ^{o}C, respectively, at T2, and 0.66 vs 0.68 ^{o}C, respectively, at T3. The model, however, over-estimates the magnitudes of low frequency variability at both locations, as reflected in the differences between modeled and observed standard deviations (Table 2).

The model and observed N-S velocities at T2 agree on the short-term variability in terms of both mean values and the amplitude of variability (Figure 5c, e; Table 2). Moreover, in the

upper layer modeled N-S velocity strongly correlates with observed values (e.g. r=0.66 at 68 m). However, the model-data correlation decreases with depth. Both model and observed E-W velocities show a persistent eastward component, but the model average is only about 50-60% of the observed (Figure 5 d, f; Table 2). Also, the observed E-W velocity shows much stronger variability than the modeled. Comparisons of modeled and observed currents at other depths above this same location, and at two other mooring sites, yield similar conclusions (not shown).

As another check on modeled vertical structures of water properties, we compared model and observed temperature and salinity profiles at several stations over the Pourtalès Terrace during the FloSEE survey (Table 2). Modeled temperature agrees well with these measured data, with a correlation coefficient r=0.97. However, the model-data agreement for salinity is less strong (r=0.75). In particular, the model under-estimates salinity by 0.3-0.6 psu in the upper 150 m. Modeled chlorophyll profiles show a prominent subsurface chlorophyll maximum (SCM) at all of the FloSEE stations, which depth is quite variable between stations. No direct comparison, however, was made for the modeled chlorophyll with FLOSEE data, which only reported fluorescence. The observed fluorescence, however, shows a consistent depth of maximum at ~65 m.

For all of these comparisons, model skills are quantitatively evaluated with three metrics: correlation coefficient (r), standard deviation (std), and normalized root mean squared error (RMSE). These can be summarized with the Taylor diagram as shown in Figure 6 (Taylor, 2001). Here "A" is the reference point representing the perfect match between model and data, and other letters represent the cases evaluated (Table 2). The closer the triad is to "A" the better model skill. It is clear that the poorest agreement is from the comparison with mooring data (cases K-P), indicating the challenge of the model in reproducing both the phase and magnitude

of the temporal variability on small scales. Overall, this diagram indicates a reasonable performance of the model.

3.2. Upwelling driven by Florida Current and mesoscale eddies

Florida Current typically tilts up to the left flank due to the bottom Ekman transport and associated geostrophic adjustment (Figure 4). In a steady state, bottom friction acting on the current would lead to bottom Ekman transport, which moves to the left of the current and drives near bottom upwelling of nutrient-rich cold waters up the slope (Hsueh and O'Brien, 1976; Garrett et al. 1993; Seim et al. 1999: Zhang et al. 2017). Thus upwelling or downwelling due to current meandering and eddies will be superimposed on this background because variability in the Florida Current or the presences of eddies will change bottom Ekman transport, leading to enhanced upwelling or reduced upwelling, i.e. downwelling. Moreover, upwelling generally accompanies strong and persistent phytoplankton blooms near the slope area (e.g. Llopiz, 2008), which is also seen from our model results (not shown). The export of the organic matter produced in these blooms can be critical food sources for the abundant deep corals found in the Straits.

The formation and evolution of mesoscale and sub-mesoscale eddies associated with the FC have been well documented (e.g., Lee, 1975; Lee and Mayer, 1977; Lee et al. 1995; Fratantoni et al. 1998; Kourafalou and Kang, 2012; Richardson et al. 2015). Elongated mesoscale and sub-mesoscale eddies with low temperatures near their cores are frequently produced locally or pass through this area. Elevated chlorophyll concentrations are frequently observed along the edge and near the center of these eddies using satellite images (e.g. Kourafalou and Kang, 2012). This model is able to produce similar mesoscale and sub-

421 mesoscale eddies in the Straits, although sub-mesoscale activities might be under-represented in
422 the model because of its relatively coarse model resolution (1.5 km). We will focus on mesoscale
423 eddies in the following sections.

424 Modeled results suggest mesoscale eddies could have significant impacts on bottom
425 water properties over the Pourtalès Terrace. As an example, we present a series of currents maps
426 at 150 m and bottom temperature over the Pourtalès Terrace (Figure 7, left), as well as the
427 companion vertical distributions of temperature and along-channel (W-E) velocity along the ~
428 81°W transect across the shelf slope of Pourtalès Terrace (Figure 7, right). Between February 16-
429 25, 2012, a mesoscale eddy passes through the area (Figure 7c, e, g). On Feb. 4, 2012, before the
430 eddy, bottom temperature and 150 m currents indicate persistent cross-slope transport at the
431 western end of the Pourtalès Terrace, leading to cold waters (~10^{o}C) residing over the inner side
432 of the platform (Figure 7a, b). This is in addition to the upwelling driven by the bottom Ekman
433 transport induced by the Florida Current, as noted above. As a result, bottom temperature over
434 the outer slope of the terrace is typically warmer than on the platform. On Feb. 16, 2012, an eddy
435 is seen encountering the western edge of the terrace, which appears to have blocked cold-water
436 intrusion onto the inner platform, but instead brings deep water directly through the outer slope
437 (Figure 7c, d). The eddy takes about one week to propagate through the terrace. Both the leading
438 front and eddy center drive strong upwelling, uplifting the isopycnals and flushing the terrace
439 with deep cold waters (Figure 7e, f). After the eddy passes through the area, significant
440 downwelling takes place along the trailing edge of the eddy, which flattens the thermocline and
441 the western part of the terrace is covered with warmer waters (~16^{o}C) (Figure 7g, h). Thus, the
442 temperature change over the terrace before and after the passage of the eddy is 3-7^{o}C. A
443 examination of model results over the two-year period suggest that similar events have happened

444 3 times in 2011 and 4 times in 2012, all occurring during spring and fall seasons.

445

446 **3.3. Island wakes around the Miami Terrace**

447 The dynamics of currents-bathymetry interactions over the Miami Terrace is different
448 from those over the Pourtalès Terrace. This can be illustrated with a series of temperature and
449 currents maps at 300 m (Figure 8, left panels) and temperature and N-S water velocity maps
450 along a cross-slope transect at 25°25´N (Figure 8, right panel) for February 14-24, 2012. In this
451 area, the Florida Current changes its direction from northeastward to northward, and therefore
452 the current axis often meanders significantly. In the upper layer, however, the Florida Current
453 typically follows the nearly straight N-S shelf slope. Thus, strong upwelling is primarily due to
454 the bottom Ekman transport. In deeper areas, the bathymetry contour takes a sharp turn from
455 northeast to north at around 25°12´N, and then another turn to the east at around 25°45´N. As a
456 result, the left flank of the Florida Current frequently overshoots, creating island wakes with an
457 area of low flow and significant upwelling over the Pourtalès Drift, an area between 25°N and
458 the Miami Terrace (Figure 8 c-f). Consistent with our results, Kourafalou and Kang (2012) also
459 found that stronger upwelling takes place in this area as the core of the current shifts eastward
460 away from the western slope. Unlike their analysis, which focused on the top 200m, our focus
461 here is deeper areas.

462 Clearly, the upwelled cold deep waters will be transported downstream toward the terrace.
463 This effect can be illustrated in Figure 9, which shows the maps of bottom temperature and
464 currents (Figure 9, left panels) and temperature and N-S velocity along a cross-slope transect at
465 the south end of the Miami Terrace (25°40´N) (Figure 9, right panel) during the same period as
466 in Figure 8. It is notable that the overshoot of Florida Current on February 18, 2012 leads to a

467 cyclonic eddy of approximately 20 km wide and 50 km long in the wakes along with strong
468 upwelling that further uplifts the thermocline (Figure 9c, d). The eddy propagates slowly
469 downstream but only lasts a few days, disappearing within a 30-40 km distance of the spawning
470 area (Figure 9e, f). An examination of modeled results over the 2-year period indicates frequent
471 occurrences of this eddy, approximately once per week each lasting about 2-5 days.
472 The occurrence of this eddy significantly affects the bottom water properties over the
473 Miami Terrace. Without an eddy, bottom water temperature on the platform is typically 2-4^{o}C
474 warmer than over the slope (Figure 9a, b). When an eddy is present, both the isothermals over
475 the center and along the leading edge of the eddy are further uplifted (Figure 8d, f and 9d, f),
476 allowing more upwelling of cold waters over the platform and reducing the bottom temperature
477 (Figure 9c, f). As the eddy propagates downstream, it induces significant downwelling of warmer
478 upper layer waters in its wake (Figure 9g, h). Sometimes, a return flow at between 200-300 m
479 water depth is present, likely due to the geostrophic adjustment. Soloviev et al. (2017) also noted
480 the presences of an intermittent countercurrent down to 244 m over the Miami Terrace.
481 Island wakes and associated upwelling of deep cold waters are ubiquitous phenomena
482 when oceanic currents encounter topographic obstacles in the deep oceans (e.g. Dong et al. 2007).
483 In our case, this is largely a subsurface phenomenon because the wakes and eddy are mostly
484 below the thermocline. Several previous studies have reported that a countercurrent (southward)
485 existed between 400-700 m and 25^{o}40'N-25^{o}50'N based on data collected at moorings and from
486 AUV surveys (Düing and Johnson, 1971; Lee and Moore, 1977; Correa et al. 2012). The
487 maximum speed of the countercurrent can sometimes exceed 50 cm/sec and the current can
488 extend vertically about 200 m above the bottom. Submersible dives on the coral mounds at the
489 foot of the terrace show that their steeper slopes and live coral colonies tend to occur on the

northern slopes of the mounds (Correa et al. 2012). This is evidence of fairly persistent southerly currents as elsewhere in the Straits, the coral growth is on the current-facing south slopes of the mounds. Our model results, however, do not show such a persistent countercurrent. Rather, reverse currents on the western side of transient eddy occur frequently over a broad area between 400-700m and spanning 20-30 km in N-S distance. However, these earlier surveys are either relying on spatially sparse stations (Lee and Moore, 1977) or limited to small areas of AUV mapping or a few mooring stations. Thus while it is possible that the model missed producing this countercurrent, another possibility is that what they observed is the return currents along the west side of a cyclonic eddy.

3.4. Bottom DIC and TA distributions

Modeled variability of near bottom carbonate chemistry is closely associated with the physical processes, particularly upwelling of deep cold waters. In fact, the bottom DIC pattern largely mirrors bottom temperature, while bottom TA pattern largely follow temperature because of the nearly opposite relationships between TA and DIC to temperature in these waters, i.e. lower temperature corresponding to lower TA but higher DIC, within the range of the bottom temperature in these areas ($8^oC<T<16^oC$) (Figure 2b, c). We focus on bottom and cross-sectional DIC distributions on the Pourtalès Terrace and Miami Terrace during the same periods as shown in Figures 7-9 (Figures 10-11).

During normal situations without the presences of eddies, cold DIC-rich waters cover most of the Pourtalès Terrace, with the exception being the southeastern flank due to persistent upwelling noted above (Figure 10a, b). The passage of a mesoscale eddy clearly brings more deep water onto the terrace, increasing the spatial coverage of high DIC waters including

513 flooding the southeastern part of the terrace (Figure 10e, f). After the eddy passes, downwelling
514 brings warm and reduced DIC waters over western part of the terrace (Figure 10g, h). In the
515 deeper areas (>400 m) where temperature is lower than 12ºC, however, there is little change in
516 DIC concentration over time and space (Figure 10, right panels). This is because within this
517 temperature range (4-12ºC) waters are within the salinity minimum zone (Figure 2a) and both
518 DIC and TA concentrations are in the neighborhood of their local extrema with a narrow range
519 of variations (< 25 µmol/kg).
520 Over the Miami Terrace, bottom DIC concentrations are also closely associated with
521 bottom temperature following the development of island wakes and the upwelling of deep cold
522 waters (Figure 11). When the transient eddy is not present, upwelling is already strong and high
523 DIC waters cover much of the terrace, but the outer edge of the platform is covered by relatively
524 warmer water with lower DIC concentration (Figure 11a, b). When an eddy is formed in the
525 wakes, strengthened upwelling brings up more cold DIC-rich waters and the entire terrace is
526 flushed with high DIC waters (Figure 11c-f). Similarly, the downwelling after the passage of the
527 eddy reduces the DIC concentrations over the much of the terrace (Figure 11g, h). Yet again,
528 there is little change (<10 µmol/kg) in DIC concentrations over the deeper areas (> 400m) where
529 temperature is lower than 12ºC (Figure 11, right panels)
530
531 **3.5. Temporal variability of bottom water properties**
532 In order to understand the temporal variability of bottom water properties, we chose four
533 representative locations, one on the platform (160 m) and another on upper slope (296 m) (below
534 the platform) of the Pourtalès Terrace, one on the platform (280 m) and another on the upper
535 slope (417 m) of the Miami Terrace (Figure 1). The time-series of T, S, DIC and TA

concentrations, and aragonite saturation at these locations are shown in Figure 12. The modeled results suggest somewhat larger ranges of temperature (8-17.9^{o}C) on top of the platform than that (8.2-14.2^{o}C) over the upper slope over the Pourtalès Terrace (Figure 12a, b). The salinity shows a similar range (35.1-35.8 psu) at both locations. It is interesting to note that bottom temperature on the platform of the Pourtalès Terrace is normally lower than that over the upper slope area throughout the modeling period, except during a few episodic events. Spatially, the warmer area generally covers the southeast part of the terrace between 200 m and 400 m isobaths (Figure 7a, c). A close examination indicates most of the events are due to the passage of mesoscale eddies, which first induce strong upwelling along the leading fronts to greatly reduce the bottom temperature over the upper slope (Figure 7c-f) and then drive strong downwelling along their trailing edges to greatly increase temperature on the platform (Figure 7g, h). The bottom temperature and salinity changes during these events can be up to 6^{o}C and 0.6 psu, respectively, at both locations.

In comparison, both bottom temperature and salinity on the platform of the Miami Terrace also show strong temporal variability, with a temperature range of 6-14.5^{o}C and a salinity range of 34.9-35.9 psu (Figure 12a, b). Overall, waters at this location are 2-4^{o}C colder and fresher than waters on both the platform and upper slope of Pourtalès Terrace, even though the water depth here is comparable to the upper slope site of Pourtalès Terrace, suggesting stronger impacts of upwelling due to the island wakes and associated eddies. At the deeper site (417 m), both temperature and salinity are very stable, showing little changes over time ($6^{o}C<T<9.7^{o}C$, $34.9<S<35.3$). Bottom temperature and salinity at the two sites on the Miami Terrace are quite similar, except during a few downwelling events when temperature and salinity on the platform increase up to 6^{o}C and 0.75 psu and during a prolonged warm period 2012 from

559 mid August through the end of November. Those downwelling events typically last from a few
560 days to more than 1 week, mostly due to the passage of transient eddies spun off from the island
561 wakes.

562 The temporal variability of near bottom DIC and TA concentrations are also closely
563 associated with water movements as seen in Figures 7-10 (Figure 12c, d). Both DIC and TA
564 concentrations on the platform of Pourtalès Terrace show a wide range on short-term (~weekly),
565 2,140-2,210 μmol/kg for DIC and 2,305-2,360 μmol/kg for TA, respectively. In contrast, both
566 DIC and TA show much narrower ranges, <30 μmol/kg, over the upper slope of the Pourtalès
567 Terrace. Consistent with the variability of bottom temperature, bottom DIC/TA concentration on
568 the platform is normally higher/lower than that over the upper slope area throughout the
569 modeling period, except during a few episodic events such as when an eddy passes through the
570 area. This is consistent with the spatial pattern seen in Figure 10a and 10c, which show that
571 waters with relatively low DIC concentration covers much of the southeastern part of the terrace
572 between 200 m and 400 m isobaths. Coincidently, this relatively low DIC area overlaps with
573 most of the NOAA designated HAPC for the Pourtalès Terrace (e.g. Reed et al. 2013). On the
574 platform of the Miami Terrace, DIC and TA concentrations show somewhat larger ranges (45
575 μmol/kg for DIC and 35 μmol/kg for TA) than those on the upper slope of Pourtalès Terrace. On
576 the upper slope of the Miami Terrace, both parameters are fairly stable with a narrow range <10
577 μmol/kg throughout the modeling period. In deep areas (> 400 m), bottom values of these two
578 parameters are effectively constant throughout the Straits as shown in Figures 10-11.

579 A simply correlation analysis of these time-series indicates that temperature alone
580 explains > 76% of low frequency variability in bottom DIC and TA in these areas, except for the
581 upper slope of Miami Terrace (56% for both DIC and TA). For short-term (high frequency)

582 variability, temperature explains >64% of DIC and TA short-term variability for the two sites on
583 the platform of the Pourtalès Terrace and Miami Terrace (see Table 3). The correlations between
584 high frequency T and DIC variability for the two upper slope sites of the terraces are either weak
585 or non-existent, reflecting the low DIC range (<15 μmol/kg) for these water masses (Figure 2b).
586 In contrast, the T-TA correlation for the high frequency variability remains strong (r=0.92) on
587 the upper slope of the Pourtalès Terrace. However, it is significantly weaker at r=0.69 on the
588 upper slope of the Miami Terrace.
589 We note that these ranges of temperature variations, particularly at those stations on top
590 of the platforms of both terraces may be somewhat exaggerated. Based on the model-data
591 comparisons at the T2 and T3 mooring stations and assuming the model performances over these
592 two terraces are similar, we can roughly estimate the variability of bottom temperature
593 (measured with the standard deviation) at the two stations on top of the platforms (PT-160m and
594 MT-280m) are roughly over-predicted by 20-30%. However, we do not have data to gauge the
595 performance of temperature simulation in deeper areas. Given the modeled temperature ranges
596 are smaller in these areas, we shall expect less model biases from the modeled temperature at the
597 two deeper stations (PT-296m and MT-417m). Both DIC and TA show nearly linear
598 relationships with the temperature within the modeled temperature ranges at the two stations on
599 top of the platforms (PT-160m and MT-280m). Thus the over-predictions of DIC and TA ranges
600 at these two stations are likely similar to that of temperature, at 20-30%. In deeper areas (PT-
601 296m and MT-417m), both the DIC and TA relationships with temperature are much weaker,
602 within the temperature ranges (6-12^{o}C) at these depths (see, e.g. Figure 2). Therefore, we shall
603 expect the model over-prediction of DIC and TA ranges in these areas are likely small.

604 The temporal variability of T, DIC, and TA over the Pourtalès Terrace leads to significant
605 variability in Ω_{Ar}, with the annual range between 1.2-2 (Figure 11e). On top of the Miami
606 Terrace, Ω_{Ar} shows a similar pattern but with a smaller annual range, between 1.2-1.7. On the
607 upper slope of the Pourtalès Terrace the Ω_{Ar} ranges 1.3-1.6, whereas on the upper slope of the
608 Miami Terrace and all of the deeper area (>400 m) Ω_{Ar} is nearly constant, between 1.2-1.3
609 throughout the year. The narrow range of Ω_A for deep waters is associated with the narrow
610 ranges of TA and DIC concentrations around the salinity minimum. Interestingly, Ω_{Ar} is also
611 strongly correlated with temperature (r>0.81) for both low and high frequencies at all of the sites
612 except for the upper slope site of the Miami Terrace, where the correlation is strong at low
613 frequency (r=0.74) but much weaker for high frequency (r=0.57) (Table 3). As noted above, the
614 variability of the key variables (T, DIC, TA) for Ω_{Ar} is somewhat over-predicted. For the two
615 shallower stations (PT-160m and MT-280m), assuming a 20% over-prediction of temperature,
616 DIC and TA variability (measured as std, see Table 1), a simple calculation using CO2SYS
617 (Lewis and Wallace, 1998; Van Heuven et al. 2011) suggests that the variability of Ω_{Ar} may have
618 also been over-predicted by ~20%. For the two deeper stations (PT-296m and MT-417m),
619 assuming a 10% over-prediction of temperature would mean <5% over-prediction of DIC and
620 TA variability because the DIC-T and TA-T relationships are mostly flat for the temperature
621 ranges experienced at these stations (6-12^{o}C). Therefore, we shall expect the predicted ranges of
622 Ω_{Ar} at these stations are fairly close to the actual range because small change in temperature
623 alone does not change Ω_{Ar} very much. In brief, variability of water masses over these terraces
624 driven by meso-scale eddies and FC meandering are strongest during spring and fall of the model
625 period, and their impacts on the Ω_{Ar} variability are significant for the areas on top of the terraces
626 but likely small for deeper areas.

627

628 **3.6. Bottom distribution of aragonite saturation state (Ω_{Ar})**

629 To further understand the bottom carbonate chemistry in these deep coral habitats, we
630 present the annual mean bottom Ω_{Ar} value and its standard deviation for 2012, which were
631 computed based on the daily bottom Ω_{Ar} derived from bottom temperature, salinity, DIC and TA
632 (Figure 13). The results for 2011 are very similar (not shown). Model results indicate dynamic
633 upper slope regions including the platform and upper slope areas, where FC meandering, eddies,
634 and associated upwelling/downwelling all contribute to the variability of bottom water properties,
635 and relatively stable lower slope regions. On top of the platforms of both terraces (between
636 approximately 200-400 m), Ω_{Ar} is typically higher than 1.4. Due to the presence of deep cold
637 waters, Ω_{Ar} is relatively low over the inner platform of Pourtalès Terrace and southern Miami
638 Terrace. In contrast, the Ω_{Ar} value over the southeastern part of Pourtalès Terrace and northern
639 part of Miami Terrace is significantly higher. These are the areas less affected by upwelling
640 driven by bottom Ekman transport and island wakes, as discussed above. On average, the slope
641 regions for the two terraces experience low to moderate aragonite saturation, between 1.4 and 2
642 (Figure 12a). Consistent with the variability of bottom water properties, aragonite saturation on
643 the platforms of both terraces and over the upper slope (<400 m) regions shows much more
644 variability than in deeper areas (Figure 13b).

645

646 **4. Discussion**

647 The modeled results indicate that the variability of bottom water properties including
648 carbonate chemistry in the Florida Straits, particularly over the two deep coral habitats, is
649 strongly affected by the movements of deep waters such as upwelling and downwelling. These

upwelling and downwelling events are due to mesoscale processes and meandering of the Florida Current, and are also influenced by water properties in the source waters. In the following, we first discuss the bottom water masses in the Florida Straits, and then evaluate the respective roles of mesoscale eddies, large-scale transport, and biogeochemical processes in these variability.

4.1. Bottom water masses over the deep coral habitats

Water masses in the Florida Straits are ultimately derived from the Caribbean Current, which becomes the LC as it enters the GOM through Yucatan Channel (Rivas et al. 2005). The LC either flows directly into the Florida Straits or loops into the northern GOM. Its recirculation loop impinges on the Florida Shelf near the Dry Tortugas (Gordon, 1967) and becomes the FC in the southern Straits of Florida. Therefore, depending on the mode of the Loop Current, water properties in the FC may more closely resemble GOM waters or Caribbean waters. To date, there are no reported measurements for DIC and TA concentrations in the Caribbean waters. Thus, we assume that their values are similar to those observed in the northern GOM (Figure 14, also see Figure 2).

Based on the T-S diagrams for the GOMECC2 survey along the WFL and EFL transect and our modeled results at the four chosen sites over the two deep coral habitats, it is clear that bottom waters over these habitats primarily comprise of two types of water masses: the North Atlantic central water (NACW) ($10^oC<T<16^oC$, $35.2<S<36.4$) and the GOM Central Waters (GOMCW) ($6^oC<T<10^oC$, $34.9<S<35.3$) (Figure 14a). The GOMCW is lying beneath the NACW and its origin can be traced back to AAIW (Atkinson, 1983). In deeper (>400m) areas, however, it seems that the water mass is primarily from the GOMCW. In both the GOM and the Straits, above the NACW, is the North Atlantic Salinity Maximum Water (SMW) (S>36), which

673 is not present in the bottom waters over these coral habitats. These water properties are largely
674 consistent with the water masses observed at the stations between 10-20°N along the WOCE A20
675 transect in summer 1997. However, salinity in the AAIW observed along A22 is about ~0.15 *psu*
676 lower than that in GOMECC2 cruise, suggesting either change in the source waters or
677 modification along the transit path from the western tropical Atlantic Ocean (within North
678 Brazilian Current) through the Caribbean Seas.
679 The modeled TA and DIC concentrations over these deep coral habitats are largely
680 consistent with those observed along the GOMECC2 WFL and EFL transects (Figure 14b, c).
681 Modeled DIC concentration on the platform of Pourtales Terrace, however, is about 0-15
682 μmol/kg higher than those observed along the two GOMECC2 transects, suggesting local
683 enrichment. Also, consistent with water mass changes between WOCE A22 transect and
684 GOMECC2 observations noted above, the GOMCW has about the same DIC concentration, but
685 ~5-10 μmol/kg higher TA concentrations.
686 The Loop Current penetrated deeply into the northern GOM during most of 2011-2012,
687 except during summer-fall 2012, based on the satellite altimetry
688 (https://www.aviso.altimetry.fr/en/my-aviso.html). Therefore, CO_2 concentrations in both
689 NACW and AAIW are likely further increased as a result of remineralization of organic matter
690 from the GOM shelf waters (Wang et al. 2013; Wanninkhof et al. 2015). Once entering the
691 Florida Straits, the waters are compressed upward as the current passes through the Straits due to
692 the dramatic shoaling (>1000 m within a distance of <200 km) of bottom topography. The low
693 temperature and high DIC NACW and AAIW waters are further steered upward over the slope
694 of the left flank due to FC meandering and eddies while being transported through the straits as
695 noted above. These explain the modeled results that bottom water masses over the upper portion

696 of these coral habitats, despite being relatively shallow <400 m, are comprise primarily of
697 NACW and AAIW, whereas bottom waters over the deep areas > 400 m are primarily from the
698 AAIW (Figure 14).
699 Global models have suggested that the equatorial North Atlantic will experience shoaling
700 of aragonite saturation horizon (ASH) in the future due to the ocean acidification (Orr et al.
701 2005; Orr, 2011). Higher CO_2 concentrations are present in the AAIW because high
702 anthropogenic CO2 uptake in the Southern Ocean (Sabine et al. 2004; Gruber et al. 2019)
703 contribute to ocean acidification in the Straights . Given the close correlation of bottom water
704 properties in the Straits with the GOMCW and AAIW, ocean acidification will likely greatly
705 shift the bottom carbonate chemistry in these areas including more frequent low aragonite
706 saturation and will possibly breach the Ω_{Ar}=1 threshold. Moreover, a recent study indicates that
707 the Atlantic meridional overturning circulation will provide a fast track delivery of acidified cold
708 waters through high latitude deep-water formation and subsequently spreading over the deep
709 oceans (Perez et al. 2018). This implies that the deep coral reefs in our study region may
710 experience more stress due to the lower availability of carbonate ions. However, potential
711 impacts of lowering Ω_{Ar} on deep corals remains poorly understood (e.g. Hoegh-Guldberg et al.
712 2017). So far, there are only limited direct experiments testing the effects of ocean acidification,
713 mostly focusing on calcification rates, and these results are mixed (e.g. Maier et al. 2009, 2012;
714 Form and Riebsell, 2012; Lunden et al. 2014; Georgian et al. 2016a). Low Ω_{Ar} may also affect
715 other aspects of deep corals including reproduction, larval growth and dissolution of dead
716 skeleton. Yet, the exact effects of these are largely unknown.
717 Warming temperature, and deoxygenation are also expected as a result of global warming
718 (Lunden et al. 2014), both of which will potentially add to the stress to deep corals. Global

719 warming may also lead to a reduction in the volume transport of Florida Current as a result of the
720 weakening north Atlantic meridional overturning circulation (Caesar et al. 2018). This could
721 potentially lead to weaker interactions between Florida Current and the bathymetry, and the
722 nonlinear instability, both in turn likely lead to reduced upwelling and less vigorous mesoscale
723 activity. It is not immediately clear how increased vertical stratification of Florida Current may
724 affect upwelling or mesoscale processes.
725
726 **4.2. Mesoscale eddies versus large-scale processes**
727 Several processes are involved in the current- and eddy-topography interactions and deep
728 water transport over the Pourtalès and Miami Terraces. All of these processes are operating on
729 the background of persistent upwelling due to bottom Ekman transport (Hsueh and O'Brien,
730 1976; Garrett et al. 1993; Weisberg and He, 2003; Roughan and Middleton, 2004) and also
731 topographic steering due to the alongshore changes of bottom topography (e.g. Janowitz and
732 Pietrafesa, 1982; Gula et al. 2015a, b). Furthermore, much of this also depends on the position
733 and orientation of the Florida Current. Kourafalou and Kang (2012) suggested that eddy
734 formation in the southern Florida Straits is strongly tied to the latitudinal position of the Florida
735 Current. Over the Miami Terrace, our modeled results suggest that the dominant mesoscale
736 process is the island wakes and associated transient eddy production. The island wakes and eddy
737 formation, however, are also likely largely modulated by the meandering and strength of Florida
738 Current. Taken together, these results indicate the importance of large-scale processes in
739 modulating bottom water properties over these deep coral habitats.
740 The relative effects of large-scale processes and eddies in driving the upwelling or cross-
741 shelf transport, however, have not been quantified. Here, we explore this quantitatively through a

742 correlation analysis between the bottom temperature and relative vorticity (at mid-depths) on the
743 Pourtalès Terrace and Miami Terrace (Figure 15). Here we show the results for the two upper
744 slope sites. The results for the shallower sites are similar, but more complicated due to transport
745 of upwelled waters from upstream. We used a Lanczos low-passed filter to split the variability of
746 these two parameters into high-frequency (<11 days), which is assumed to be due to mesoscale
747 processes the most significant of which is eddies, and low-frequency (>11 days), which is largely
748 due to the variability of the Florida Current position and transport. An 11-day cut-off is a
749 somewhat arbitrary choice as the time-scale separating the low and high frequency. This kind of
750 partition is commonly used, but does not completely isolate mesoscale effects because the FC
751 meandering may indirectly affect mesoscale activities or vice versa (Kourafalou and Kang, 2012).
752 It is worth noting that a previous study indicated that the Florida Current meandering has two
753 dominant periods, 5 and 12 days (Johns and Schott, 1987) in the northern Florida Straits. Meinen
754 et al. (2010) indicated that significant energy for the variability of FC transport lies within the
755 periods of <10 days. A longer cut-off time, e.g. 15-day, does not significantly affect the results of
756 our analysis below (see Figure S3).
757 It is clear that both low frequency FC variability and mesoscale processes contribute
758 positively (negative correlation) to the upwelling of cold waters onto the Pourtalès Terrace. The
759 FC meandering, however, shows somewhat stronger impacts than the eddies on the bottom
760 temperature variability (r=-0.59 versus r=-0.39, respectively). By contrast, the upwelling over
761 the Miami Terrace is positively correlated to the relative vorticity (the longitudinal position), i.e.,
762 when the current core moves closer to the terrace (higher relative vorticity) the near bottom
763 temperature is higher, and vice versa (r=0.57). Similar influences on temperature anomaly come
764 from short-term processes due to the effects of island wakes and the transient eddy (positive

765 correlation r=0.58). More specifically, high anomaly of relative vorticity (positive anomaly)
766 indicates that the FC is close to the slope and that there is a lack of wakes associated with the
767 positive temperature anomaly (a lack of upwelling). On the contrary, negative vorticity anomaly
768 indicates a well-developed island wake, or the presence of the transient eddy, associated with
769 strong upwelling (negative temperature anomaly).

770 These results suggest the important roles of both local physical processes and remote
771 forcing on the bottom carbonate chemistry, which is strongly correlated with the bottom
772 temperature, particularly for the low frequency variability and/or areas over the platforms (Table
773 3). However, impacts become nonlinear when upwelling is strong and near bottom cold waters at
774 the base of the slope are upwelled to mid-slope due to the nonlinear T-DIC and T-TA
775 relationships at the low temperature end for AAIW (Figure 2). On the other hand, changes of
776 water properties (T, S, TA, DIC) in the source areas, GOM or Caribbean Seas, will affect the
777 bottom water properties in the Florida Straits. The impacts of these, however, are likely largely
778 on the low frequency variability. There is a significant but weak correlation (r<0.6) between the
779 bottom water temperature over both the habitats and subsurface temperature in the Gulf on the
780 low frequency time-scale (>11 days), whereas no significant correlation is found for high
781 frequency signals (not shown).

782

783 **4.3. Contributions of biological export and remineralization to bottom carbonate chemistry**

784 Biological processes including phytoplankton photosynthesis, remineralization of organic
785 matter, and calcification could also contribute to the change of total CO_2 and alkalinity in the
786 water column (see, e.g. Wanninkhof et al. 2015). Here we only consider the phytoplankton
787 photosynthesis and remineralization, which would, respectively, decrease and increase DIC by 1

788 μmol/kg per μmol/kg uptake or remineralization. Assuming these processes follow a 6.625 C/N
789 Redfield ratio for photosynthesis and remineralization, photosynthesis (remineralization)
790 incorporating (releasing) nitrate would slightly increase (decrease) alkalinity by 1/6.625 μmol/kg
791 per μmol/kg carbon change. Phytoplankton photosynthesis is low with phytoplankton biomass
792 being typically < 4 μmolC/l (chlorophyll < 1 μg/l) due to the limitation of low dissolved
793 inorganic nitrogen concentration in the upper layer (e.g. Llopiz, 2018; Figure S2). Therefore, the
794 variability of this term is unlikely a major factor to the variability of water column DIC
795 concentration. For near bottom waters over these deep coral reefs, there is no photosynthesis and
796 only remineralization of organic carbon takes place. Our model results indicate that particulate
797 organic carbon (POC) concentration in the deep waters is typically an order lower than the
798 dissolve organic carbon (DOC) concentration (not shown). This is consistent with the observed
799 POC concentrations in the upper 150 m along a cross-slope transect off Jacksonville, FL, about
800 100 mile north of our northern boundary during the July 2015 ECOA cruise, which indicate a
801 range of 2-6 μmolC/kg ((https://www.nodc.noaa.gov/oads/data/0157080.xml). Therefore the
802 overall contribution of POC remineralization to DIC is small. As for the DOC contribution,
803 during the transit from the upstream boundary in the Gulf of Mexico to the southern Florida
804 Straits, we shall expect an increase of DIC by,

805 $$\Delta DIC = r_{DOC} DOC * \Delta t, \quad (1)$$

806 where r_{DOC} is the remineralization rate and Δt is the transit time. The measured DOC
807 concentration was at 40-60 μmol/kg along the EFL transect during the GOMECC-2 survey.
808 Hansel et al. (2004) reported a similar range of 40-50 μmol/kg along the same transect during a
809 survey in January-February, 1998. Leichter et al. (2007) surveyed several transects from the
810 Keys to offshore up to 250 m water depth in September 11-19, 2003 and reported DOC

concentrations between 40-55 μmol/kg for waters with temperature between 12-15°C. Therefore it seems reasonable to assume that near bottom DOC concentration has a range of 40-50 μmol/kg. Our model results indicate that the near bottom DOC concentration in this area is ~30-40 μmol/kg (not shown), which is lower than the observed value. Based on our model, it takes about 5-10 days for GOM water to transit from the model GOM boundary to the Pourtalès and Miami Terrace area. We assume r_{DOC}=0.01-0.03 day^{-1} at 10°C water temperature, which is lower than the 0.03 day^{-1} used in Fennel et al. (2006). Therefore, based on equation (1) and assuming DOC=40 μmol/kg, we shall expect an increase of DIC ~ 4-10 μmol/kg during the transit from the GOM. During the same transit period, a small, 1-2 μmol/kg, decrease in TA is expected.

We have not included the contributions of sediment fluxes to the near bottom DIC and alkalinity, which may be significant because of active sediment diagenesis and strong sediment transport due to the strong near bottom currents, up to 50 cm/sec, that these reefs experience. Strong currents are expected to be the main mechanism for sediment input from upstream. However, little is known regarding the related benthic biogeochemical processes.

4. Summary and conclusions

A numerical model was developed to simulate the coupled physical-biogeochemical processes on the south Florida shelf and in the Florida Straits and a two-year (2011-2012) simulation was carried out. Built on previous work by Pan et al. (2017), we further gauge the model performance by comparing the model results with limited available data from two research cruises, transport measurements along 27°N, and several deployments of two ADCP moorings that took place during the model period. The results show overall agreement between model output and observations, including the magnitudes of high frequency (<11 days)

834 variability in temperature, currents and FC volume transport. However, there are also
835 discrepancies including over-predicting the magnitude of the temporal variability of water
836 properties such as a temperature at the two mooring sites, over-estimating the bottom W-E
837 velocity at the two mooring sites, and under-predicting the low frequency transport variability.
838 One possible reason for these discrepancies is that the model does not fully capture the
839 interactions of low frequency Rossby waves with the complex bathymetry in this area due to the
840 model resolution. The model reproduces the general vertical structure of key parameters (T, S,
841 TA and DIC) including the near permanent upwelling over the western slope along the 27˚N
842 transect observed during the GOMECC-2 survey.
843 Model results were then used to examine the spatial-temporal variability of key physical
844 and carbonate chemistry parameters (temperature, salinity, DIC and TA) over the Pourtalès and
845 Miami Terraces, two large deep coral reef habitats in the Florida Straits, and the associated
846 mesoscale and large-scale processes. Four representative sites were chosen for an analysis of the
847 temporal variability of bottom water properties over the two deep coral habitats. The results
848 indicate that the near-bottom carbonate chemistry over both the Pourtalès and Miami Terraces is
849 strongly impacted by the meandering of the Florida Current and associated mesoscale eddies
850 with differing effects in the two areas. As a general background, the Florida Current forces
851 strong near-bottom upwelling over the Pourtalès Terrace resulting from bottom Ekman transport.
852 As the current moves northward and gets closer to the slope, the bottom upwelling strengthens,
853 and vice versa, as reflected in the negative correlation between bottom temperature and relative
854 vorticity. Mesoscale eddies further enhance the upwelling by lifting up the thermocline along
855 their leading front and eddy center. Together, these processes bring cold CO_2-rich but low-
856 alkalinity deep waters onto the platform. The trailing edge of these eddies, however, drives

857 significant downwelling, which leads to significantly warmer temperature and lower CO_2
858 concentration on top of the platform. Over the Miami Terrace, by contrast, island wakes behind
859 the sharp topographic change and the frequent spin-off of the transient eddy over the Pourtalès
860 Drift play a dominant role in driving the upwelling of CO_2-rich deep waters. The meandering and
861 transport variability of the Florida Current together modulate the instability of island wakes and
862 the production of mesoscale eddies at the southern end of the terrace. Overall, stronger upwelling
863 is seen when the Florida Current shifts eastward away from the slope leading to lower
864 temperature and higher DIC concentration over to the upper slope and the platform. Previous
865 studies suggest the presence of a persistent near bottom countercurrent between 400-700 m in
866 this area. Our model results did not show this current. This is can be either that the model failed
867 to reproduce this current or that the return flow (southward) is part (west side) of the spin-off
868 eddy from the island wakes.
869 Modeled results suggest that the bottom water masses over the Pourtalès Terrace and
870 upper Miami Terrace comprise largely of NACW and AAIW. As a result of the complex
871 physical processes, however, bottom water properties (T, DIC, TA) on top of both the Pourtalès
872 Terrace and Miami Terrace exhibit strong temporal variability over weekly to monthly
873 timescales with a significant range of aragonite saturation state (1.2-2.0). In contrast, deeper
874 (>400 m) areas in the Florida Straits are flushed with AAIW and the bottom water properties are
875 very stable within the neighborhood of the salinity minimum and with nearly constant aragonite
876 saturation state between 1.2-1.3.
877 The bottom carbonate chemistry in the Straits is likely also significantly influenced by
878 changes in the water properties in their sources (GOM or Caribbean) through large-scale
879 transport and by the biogeochemical processes (remineralization of organic matter, sediment

880 inputs) along the paths. Our estimate suggests that remineralization may further contribute to a
881 DIC increase ~4-10 μmol/kg as waters transit from the GOM to the deep coral habitats. There is,
882 however, significant uncertainty in this estimate, and it does not take into account the possible
883 sediment fluxes of DIC and alkalinity along the transport paths, which depends on the mode of
884 Loop Current and sediment diagenesis processes. Ocean acidification in the future will likely
885 further reduce the pH and Ω_{Ar} leading to greater stress on the deep coral reef ecosystems in this
886 region. However, here we did not directly examine the potential impacts of ocean acidification,
887 which would require additional simulations incorporating the long-term ocean acidification
888 effects, and is beyond the scope of this manuscript.
889
890 **Acknowledgements:** MJ is funded by the Harbor Branch Oceanographic Institute (HBOI)
891 Foundation and Florida Atlantic University startup fund for this work. This is HBOI contribution
892 #2265. The HYCOM model output was downloaded from
893 https://hycom.org/data/gomu0pt04/expt-50pt1. We thank Dr. Chai at the University of Maine for
894 providing the CoSINE model output. The data from the GOMECC cruises were obtained through
895 funds of the NOAA Ocean Acidification Program awarded to LB and RW. Cooperative Institute
896 of Ocean Research, Exploration and Technology (CIOERT) at HBOI gratefully acknowledges
897 funding provided by NOAA Office of Ocean Exploration and Research (OER Grant #:
898 NA090AR4320073), NOAA Deep Sea Coral Research and Technology Program (DSCRTP;
899 CIOERT Project #: II-CO-DCE-6), and NOAA Office of Marine and Aviation Operations
900 (OMAO) in support of the research, ship time, and ROV time. The ADCP measurements used
901 for this project were conducted by the Southeast National Marine Renewable Energy Center with

902 support from the U.S. Department of Energy under award DE-EE0000319. Three anonymous
903 reviewers provided thoughtful comments and suggestions that greatly improved the manuscript.
904

905 **References**

906 • Anthony K.R.N, J.A. Maynard, G. Diaz-Pullido, P.J. Mumby, P.A. Marshall, L. Cao and O.
907 Hoegh-Guldberg, 2011, Ocean acidification and warming will lower coral reef resilience.
908 Global Change Biology 17:1798-1808.
909 • Bellwood, D.R., T.P. Hughes, C. Folke, and M. Nystrom, 2004, Confronting the coral reef
910 crisis. Nature 429(6,994), 827.
911 • Büscher J.V., A.U. Form, and U. Riebesell U. 2017, Interactive effects of ocean acidification
912 and warming on growth, fitness and survival of the cold-water coral Lophelia pertusa under
913 different food availabilities. Frontiers in Marine Science 4:101, DOI
914 10.3389/fmars.2017.00101.
915 • Caesar, L., S. Rahmstorf, A. Robinson, G. Feulner and V. Saba, 2018 Observed fingerprint of
916 a weakening Atlantic Ocean overturning circulation, 556: 191-196,
917 https://doi.org/10.1038/s41586-018-0006-5
918 • Chassignet, E.P., Hurlburt, H.E., Metzger, E.J., Smedstad, O.M., Cummings, J.A., Halliwell,
919 G.R., Bleck, R., Baraille, R., Wallcraft, A.J., Lozano, C., Tolman, H.L., Srinivasan, A.,
920 Hankin, S., Cornillon, P., Weisberg, R.H., Barth, A., He, R., Werner, F., Wilkin, J., 2009. US
921 GODAE: global ocean prediction with the HYbrid Coordinate Ocean Model (HYCOM).
922 Oceanography 22, 64-75. doi: 10.5670/oceanog.2009.39.
923 • Cohen, A.L. and M. Holcomb, 2009, Why corals care about ocean acidification – uncovering
924 the mechanism, Oceanography, 22, 118-127.

925 • Correa, T. B. S., G. Eberli, M. Grasmueck, John Reed, A. Correa. 2012. Genesis and
926 morphology of coldwater coral ridges in a unidirectional current regime. Marine Geology
927 326-328:14-27.
928 • Dickson, A. G. 1990. Standard potential of the reaction: AgCl(s) + H2(g) = Ag(s) + HCl(aq),
929 and the standard acidity constant of the ion HS04-in synthetic seawater from 273.15 to
930 318.15 K. Journal of Chemical Thermodynamics, 22:113-27.
931 • Dong, C., J. C. Mcwilliams, and A. F. Shchepetkin, 2007, Island wakes in deep water, J.
932 Phys. Oceanogr., 37: 962-981.
933 • Düing, W. and D. Johnson, 1971, Southward Flow under the Florida Current, Science, 173
934 (3995), 428-430.
935 • Fennel, K., J. Wilkin, J. Levin, J. Moisan, J. O'Reilly, and D. Haidvogel, 2006, Nitrogen
936 cycling in the Middle Atlantic Bight: Results from a three-dimensional model and
937 implications for the North Atlantic nitrogen budget, Global Biogeochem. Cycles, 20,
938 GB3007, doi:10.1029/2005GB002456.
939 • Fennel, K., J. Wilkin, M. Previdi, and R. Najjar, 2008, Denitrification effects on air-sea CO2
940 flux in the coastal ocean: Simulations for the northwest North Atlantic, Geophy. Res. Lett.,
941 L24608, doi:10.1029/2008GL036147.
942 • Form, A. U., and U. Riebesell, 2012, Acclimation to ocean acidification during long-term
943 CO_2 exposure in the cold-water coral Lophelia pertusa. Glob. Change Biol. 18, 843–853. doi:
944 10.1111/j.1365-2486.2011.02583.x.
945 • Fratantoni, P.S., Lee, T.N., Podesta, G.P., Muller-Karger, F., 1998. The influence of Loop
946 current perturbations on the formation and evolution of Tortugas eddies in the southern
947 Straits of Florida. J. Geophys. Res., 103(C11), 24,759-24,799.

948 • Garcia, R. F., and C. S. Meinen, Accuracy of Florida Current volume transport measurements
949 at 27°N using multiple observational techniques, J. Atmos. Ocean. Tech., 31 (5), 1169-1180,
950 doi:10.1175/JTECH-D-13-00148.1, 2014.
951 • Garrett, C., P. MacCready, and P. Rhines, 1993, Boundary mixing and arrested Ekman
952 layers: Rotating stratified flow near a sloping boundary. Annu. Rev. Fluid Mech., 25, 291–
953 323.
954 • Geider, R. J., H. L. McIntyre, and T. M. Kana (1997), Dynamic model of phytoplankton
955 growth and acclimation: Responses of the balanced growth rate and the chlorophyll a:
956 Carbon ratio to light, nutrient-limitation and temperature, Mar. Ecol. Prog. Ser., 148, 187–
957 200.
958 • Georgian S.E., D. Deleo, A. Durkin, C.E. Gómez, M. Kurman, J.J. Lunden, and E.E. Cordes,
959 2016b. Oceanographic patterns and carbonate chemistry in the vicinity of cold-water coral
960 reefs in the Gulf of Mexico: implications for resilience in a changing ocean. Limnology and
961 Oceanography 61:648_665 DOI 10.1002/lno.10242.
962 • Georgian S.E., S. Dupont, M. Kurman, A. Butler, S.M. Strömberg, A.I. Larsson, and E.E.
963 Cordes, 2016a, Biogeographic variability in the physiological response of the coldwater coral
964 Lophelia pertusa to ocean acidification. Marine Ecology 37:1345_1359. DOI
965 10.1111/maec.12373.
966 • Gordon, A.L., 1967, Circulation of the Caribbean Sea. *Journal of Geophysical Research*, 72,
967 6207-6223.
968 • Gruber, N., et al. (2019), The oceanic sink for anthropogenic CO2; from 1994 to 2007,
969 *Science*, *363*(6432), 1193, doi:10.1126/science.aau5153.

970 • Haidvogel, D. B. and A. Beckmann, 1999, Numerical ocean circulation modeling, Imperial
971 College Press, London, 344 p.
972 • Hoegh-Guldberg O., E.S. Poloczanska, W. Skirving, and S. Dove S, 2017, Coral Reef
973 Ecosystems under Climate Change and Ocean Acidification. Front. Mar. Sci. 4:158. doi:
974 10.3389/fmars.2017.00158
975 • Hsueh, Y. and J. J. O'Brien, 1971, Steady coastal upwelling induced by an along-shore
976 current, J. Phys. Oceanogr., 1: 180-186.
977 • IPCC, 2013, Climate Change 2013: The Physical Science Basis. Contribution of Working
978 Group I to the Fifth Assessment Report of the Intergovernmental Panel on Climate Change,
979 Stocker, T.F., D. Qin, G.-K. Plattner, M. Tignor, S.K. Allen, J. Boschung, A. Nauels, Y. Xia,
980 V. Bex and P.M. Midgley (eds.), Cambridge University Press, Cambridge, United Kingdom
981 and New York, NY, USA, 1535 pp.
982 • Janowitz, G.S., and L. J., Pietrafesa, 1982. The effects of alongshore variation in bottom
983 topography on a boundary current, or, topographically induced upwelling. *Cont. Shelf Res*.
984 1(2), 123–141.
985 • Johns, W.E. and F. Schott, 1987, Meandering and transport variations of the Florida Current,
986 *J. Phys. Oceanogr.*, 17 (8), 1128-1147.
987 • Kang, D. and E. N. Curchitser, 2013, Gulf Stream eddy characteristics in a high-resolution
988 ocean model, J. Geophys. Res.-Oceans, C118: 4474–4487, doi:10.1002/jgrc.20318.
989 • Kleypas J.A. and K.K. Yates, 2009, Coral reefs and ocean acidification. Oceanography
990 22(4):108-117.

991 • Kourafalou, V.H., Kang, H., 2012. Florida Current meandering and evolution of cyclonic
992 eddies along the Florida Keys Reef Tract: Are they interconnected? J. Geophys. Res. 117.
993 doi: 10.1029/2011JC007383.
994 • Lee, T.N., 1975, Florida Current spin-off eddies. Deep Sea Res., 22, 753-765.
995 • Lee, T.N., K. Leaman, E. Williams, T. Berger, and L. Atkinson, 1995. Florida Current
996 meanders and gyre formation in the southern Straits of Florida. J. Geophys. Res. 100, 8607–
997 8620. doi: 10.1029/94JC02795.
998 • Lee, T.N., and D. Mayer, 1977, Low-frequency current variability and spin-off eddies on the
999 shelf off southeast Florida. J. Mar. Res., 35, 193-200.
1000 • Lee, T.N. and C.N.K. Mooers, 1977, Near-bottom temperature and current variability over
1001 the Miami slope and terrace, Bulletin of Marine Science, 27(4): 758-775.
1002 • Leichter, J.J. et al. 2007, Nitrogen and oxygen isotopic signatures of subsurface nitrate
1003 seaward of the Florida Keys reef tract, Limnol. Oceanogr., 52(3), 1258–1267.
1004 • Le Hénaff, M., Kourafalou, V. H., Morel, Y., Srinivasan, A., 2012. Simulating the dynamics
1005 and intensification of cyclonic Loop Current Frontal Eddies in the Gulf of Mexico, J.
1006 Geophys. Res. 117. doi:10.1029/2011JC007279.
1007 • Lewis, E, and DWR, Wallace, 1998, Program Developed for CO2 System Calculations.
1008 ORNL/CDIAC-105. Carbon Dioxide Information Analysis Center, Oak Ridge National
1009 Laboratory, U.S. Department of Energy, Oak Ridge, Tennessee.
1010 doi:10.3334/CDIAC/otg.CO2SYS_DOS_CDIAC105.
1011 • Llopiz, J.K., 2008, The Trophic Ecologies of Larval Billfishes, Tunas, and Coral Reef Fishes
1012 in the Straits of Florida: Piscivory, Selectivity, and Niche Separation, Ph.D thesis, University
1013 of Miami. 177pp.

1014 • Lunden J.J., S.E. Georgian, and E.E. Cordes, 2013, Aragonite saturation states at cold-water
1015 coral reefs structured by Lophelia pertusa in the northern Gulf of Mexico. Limnology and
1016 Oceanography 58(1): 354_362, DOI 10.4319/lo.2013.58.1.0354.
1017 • Lunden J.J., C.G. McNicholl, C.R. Sears, C.L. Morrison, and E.E. Cordes, 2014. Acute
1018 survivorship of the deep-sea coral *Lophelia pertusa* from the Gulf of Mexico under
1019 acidification, warming, and deoxygenation. Frontiers in Marine Science 1:78 DOI
1020 10.3389/fmars.2014.00078.
1021 • Machado, P.M., J. H. VanZwieten and I. Pinos, 2016, A Measurement-Based Analysis of the
1022 Hydrokinetic Energy in the Gulf Stream, Journal of Ocean and Wind Energy, 3(1), 25–30.
1023 • Maier, C., J. Hegeman, M.G. Weinbauer, and J. P. Gattuso, 2009, Calcification of the cold-
1024 water coral Lophelia pertusa under ambient and reduced pH.Biogeosciences 6, 1671–1680.
1025 doi: 10.5194/bg-6-1671-2009
1026 • Maier C., P. Watremez P, M. Taviani, M.G. Weinbauer, J-P. Gattuso, 2012, Calcification
1027 rates and the effect of ocean acidification on Mediterranean cold-water corals. Proceedings of
1028 the Royal Society B: Biological Sciences 279:1716_1723, DOI 10.1098/rspb.2011.1763.
1029 • Mehrbach, C., C. H. Culberson, J. E. Hawley, and R. M. Pytkowicz. 1973. Measurement of
1030 the apparent dissociation constants of carbonic acid in seawater at atmospheric pressure.
1031 Limnology and Oceanography, 18: 897-907.
1032 • Meinen, C. S., M.O. Baringer, and R. F. Garcia, Florida Current transport variability: An
1033 analysis of annual and longer-period signals, *Deep Sea Research I, 57, 835-846,*
1034 *doi:10.1016/j.dsr.2010.04.001, 2010.*
1035 • Mesinger, F., et al. 2006. North American Regional Reanalysis. Bull. Am. Meteorol. Soc. 87,
1036 343-360. doi: 10.1175/bams-87-3-343.

1037 • Mienis, F. G.C.A. Duineveld, A. J. Davies, S.W. Ross, H. Seim, J. Bane, and T.C.E. van
1038 Weering, 2012, The influence of near-bed hydrodynamic conditions on cold-water corals in
1039 the Viosca Knoll area, Gulf of Mexico, Deep-Sea Res. I, 60, 32-45.
1040 • Mienis F., G. Duineveld, A.J. Davies, M. Lavaleye, S.W. Ross, H. Seim, J. Bane, H. van
1041 Haren, M. Bergman, H. de Haas, S. Brooke, and T. van Weering, 2014, Cold-water coral
1042 growth under extreme environmental conditions, the Cape Lookout area, NW Atlantic.
1043 Biogeosciences 11:2543-2560.
1044 • Mora, C., C.-L. Wei, A. Rollo, T. Amaro, A. R. Baco, et al. 2013, Biotic and Human
1045 Vulnerability to Projected Changes in Ocean Biogeochemistry over the 21st Century, PLoS
1046 Biology, 11(10): 1-14.
1047 • Orr, J. C., 2011, Recent and future changes in ocean carbonate chemistry. Ocean
1048 Acidification, J.-P. Gattuso, and L. Hansson (Eds.), Oxford University Press, p41-66.
1049 • Orr, J. C., et al. 2005, Anthropogenic ocean acidification over the twenty-first century and its
1050 impact on calcifying organisms. Nature, 437: 681-686.
1051 • Pan, C. et al. 2017, Modeling the impacts of the Loop Current on circulation and water
1052 properties over the Pulley Ridge region on the Southwest Florida shelf, Ocean Modeling,
1053 112: 48-64.
1054 • Perez, F. F. et al. 2018, Meridional overturning circulation conveys fast acidification to the
1055 deep Atlantic Ocean, Nature, doi:10.1038/nature25493.
1056 • Pietrafesa, L. 1990, Upwelling processes associated with western boundary currents. In:
1057 Phosphate deposits of the world, neogene to modern phosphorites, Burnett WC, Riggs SR
1058 (eds), vol 3. Cambridge Univ. Press, Cambridge, pp 3–26.

- Pitts P.A. and N.P. Smith, 1997, An Investigation of summer upwelling across central Florida's Atlantic coast: The case for wind stress forcing. Journal of Coastal Research, 13(1) 105-110.
- Reed J.K., S. Farrington, A. David, C.G. Messing, D.E. Guzman, and S. Pomponi, 2012, NOAA CIOERT cruise report: survey of the deep-sea coral and sponge ecosystem of Pourtales Terrace, NOAA Ship Nancy Foster, Florida Shelf-Edge Exploration II (FLoSEE) Cruise, Leg 2 - September 23-30, 2011, NF-11-09-CIOERT. 130 pages.
- Reed, J.K., S. Harter, S. Farrington, and A. David, 2014, Characterization and interrelationships of deepwater coral/sponge habitats and fish communities off Florida, USA. Chapter 5 in "Coral Habitat and Fish Interrelationships". CRC Press, p. 49-80.
- Reed, J.K., C. Messing, B. Walker, S. Brooke, T. Correa, M. Brouwer, T. Udouj, and S. Farrington, 2013, Habitat characterization, distribution, and areal extent of deep-sea coral ecosystem habitat off Florida, southeastern United States. Journal of Caribbean Science 47: 13-30.
- Reed, J.K., S. Pomponi, A. Wright, D. Weaver, and C. Paull. 2005, Deep-water sinkholes and bioherms of South Florida and Pourtales Terrace- Habitat and Fauna. Bulletin of Marine Science 77:267-296.
- Reed, J.K., D. Weaver, S.A. Pomponi, 2006, Habitat and fauna of deep-water *Lophelia pertusa* coral reefs off the Southeastern USA: Blake Plateau, Straits of Florida, and Gulf of Mexico. Bulletin of Marine Science 78(2): 343-375.
- Richardson, D.E. et al. 2009, Sailfish (*Istiophorus platypterus*) spawning and larval environment in a Florida Current frontal eddy, Progress in Oceanography, 82: 252–264.

- Rivas, D. A. Badan, and J. Ochoa, et al. 2005, The Ventilation of the Deep Gulf of Mexico, J. Phys. Oceanogr., 35: 1763-1781.
- Roberts, J.M., 2009, Cold-water coral reefs, in *Encyclopedia of Ocean Sciences*, J.H. Steele (Ed.), Academic Press, p615-625.
- Roson, G., F. Rios, F. F. Perez, A. Lavın, and H. L. Bryden, 2003, Carbon distribution, fluxes, and budgets in the subtropical NorthAtlantic Ocean (24.5ºN), J. Geophys. Res-Oceans, 108, NO. C5, 3144, doi:10.1029/1999JC000047.
- Ross S.W., S. Brooke, A. Quattrini, M. Rhode, J.C. Watterson, 2015, A deep-sea community at unusually shallow depths in the western North Atlantic Ocean off northeastern Florida. Marine Biology 162: 635-648
- Ross, S.W. and M.S. Nizinski, 2007, State of Deep Coral Ecosystems in the U.S. Southeast Region: Cape Hatteras to southeastern Florida. p. 233-270, Ch 6, In: Lumsden, S.E., T.F. Hourigan, A.W. Bruckner and G. Dorr (eds.). The State of Deep Coral Ecosystems of the United States. NOAA Tech. Memo. CRCP-3. Silver Spring, MD. 365 pp.
- Ross, S.W. and A.M. Quattrini. 2007. The Fish Fauna Associated with Deep Coral Banks off the Southeastern United States. Deep-Sea Research Part I 54: 975-1007.
- Roughan, M., Middleton, J.H., 2004. On the East Australian current: variability, encroachment, and upwelling. J. Geophys. Res. 109, C07003. doi: 10.1029/ 20 03JC0 01833.
- Sabine, C. L., et al. 2004, The Oceanic Sink for Anthropogenic CO_2*, Science, 305*(5682), 367–371
- Seim, H.E., D.P. Winkel, G. Gawarkiewicz, and M.C. Gregg, 1999, A Benthic Front in the Straits of Florida and Its Relationship to the Structure of the Florida Current, J. Phys. Oceanogr., 29, 3,125-3,132.

- Shchepetkin, A.F., McWilliams, J.C., 2005. The regional oceanic modeling system (ROMS): a split-explicit, free-surface, topography-following-coordinate oceanic model. Ocean Modelling 9, 347-404. doi: 10.1016/j.ocemod.2004.08.002.
- Smith, N., 1981, An investigation of seasonal upwelling along the Atlantic Coast of Florida. In: Ecohydrodynamics. J.C. Nihoul (ed), Elsevier, New York, pp79-98.
- Soloviev, A. V., A. Hirons, C. Maingota, C. W. Dean, et al. 2017, Southward flow on the western flank of the Florida Current, Deep-Sea Res. I, 125: 94-105.
- Stewart, A. L. and A. F. Thompson, 2015, Eddy-mediated transport of warm Circumpolar Deep Water across the Antarctic Shelf Break, Geophys. Res. Lett. 10.1002/2014GL062281.
- Thresher, R.E., B. Tilbrook, S. Fallon3, N. C. Wilson, and J. Adkins, 2011, Effects of chronic low carbonate saturation levels on the distribution, growth and skeletal chemistry of deep-sea corals and other seamount megabenthos, Mar. Ecol. Prog. Ser., 442: 87–99, doi: 10.3354/meps09400.
- Taylor, K.E., 2001, Summarizing multiple aspects of model performance in a single diagram. J. Geophys. Res., 106, 7183-7192.
- Umlauf, L., H. Burchard, 2003: A generic length-scale equation for geophysical turbulence models, *J. Marine Res.*, 61, 235-265.
- van Heuven, S., D. Pierrot, J.W.B. Rae, E. Lewis, and D.W.R. Wallace, 2011, MATLAB program developed for CO2system calculations, ORNL/CDIAC-105b, Carbon Dioxide Inf. Anal. Cent., Oak Ridge Natl. Lab., US DOE, Oak Ridge, Tenn..
- Vinick C., A. Riccobono, C.G. Messing, B.K. Walker, J.K. Reed, and S. Farrington, 2012, Siting study for a hydrokinetic energy project located offshore southeastern Florida:

protocols for survey methodology for offshore marine hydrokinetic energy projects, www.osti.gov/servlets/purl/1035555/, U. S. Department of Energy, vii + 93 pp.

- Wang, Z.A., Wanninkhof, R., Cai, W.-J., Byrne, R.H., Hu, X., Peng, T.-H., Huang, W.-J., 2013. The marine inorganic carbon system along the Gulf of Mexico and Atlantic coasts of the United States: Insights from a transregional coastal carbon study. Limnol. Oceanogr. 58, 325-342. doi: 10.4319/lo.2013.58.1.0325.
- Wanninkhof, R. 1992. Relationship between gas exchange and wind speed over the ocean. J. Geophys. Res. 97:7373–81
- Wanninkhof, R., Barbero, L., Byrne, R., Cai, W.-J., Huang, W.-J., Zhang, J.-Z., Baringer, M., Langdon, C., 2015. Ocean acidification along the Gulf Coast and East Coast of the USA. Cont. Shelf Res. 98, 54-71. doi: 10.1016/j.csr.2015.02.008.
- Weisberg R. H. and R. He, 2003, Local and deep-ocean forcing contributions to anomalous water properties on the West Florida Shelf, J. Geophys. Res 108 (C6), 3184, doi:10.1029/2002JC001407.
- Xiu, P., and F. Chai, 2014, Connections between physical, optical and biogeochemical processes in the Pacific Ocean, Prog. Oceanogr., 122, 30–53.
- Xu, X., W.J. Schmitz Jr., H. E. Hurlburt, and P. J. Hogan, 2012, Mean Atlantic meridional overturning circulation across 26.5^{o}N from eddy-resolving simulations compared to observations, J. Geophys. Res.-Oceans, 117, C03042, doi: 10.1029/2011JC007586.
- Yang, B., R. H. Byrne, and R. Wanninkhof, 2015, Subannual variability of total alkalinity distributions in the northeastern Gulf of Mexico, J. Geophys. Res-Oceans, 10.1002/2015JC010780.

Table 1. Changes of model parameters

Model parameters	Fennel et al. (2006)	This study
Light attenuation due to seawater (1/m)	0.04	0.025
PAR fraction of shortwave radiation	0.43	0.5
Inverse half-saturation for phytoplankton NO_3 uptake (1/μM)	2	1
Inverse half-saturation for phytoplankton NH_4 uptake (1/μM)	2	5
Phytoplankton natural mortality rate (day^{-1})	0.15	0.05
Maximum chlorophyll to carbon ratio (μgChl/μgC)	0.0535	0.04
Zooplankton grazing rate (day^{-1})	0.6	0.7
Half saturation constant for zooplankton grazing (μM)	2.0	0.2
Small detritus remineralization rate (day^{-1})	0.03	0.02
Phytoplankton sinking velocity (m/day)	0.1	1.0
Large detritus (PON) sinking velocity (m/day)	1.0	3.0

Table 2. Statistics for model-data comparison

Dataset	Parameter	Label	RMSE	Point-to-point correlation *	Mean±STD		Mean difference (confidence interval)*
					Model	Data	
GOMEC2	Temperature (°C)	B	2.64	**0.93**	22.15±6.5	22.45±7.38	0.3
	Salinity (psu)	C	0.34	**0.65**	36.0±0.34	36.0±0.44	0
	DIC (µm/kg)	D	20.40	**0.96**	2093.3±71.0	2085.2±76.4	**8.1 (4.3-11.3)**
	TA (µm/kg)	E	18.40	**0.69**	2367.8±20.0	2357.8±25.2	**10.0 (6.7-13.9)**
	NO_3 (µm/kg)	F	4.50	**0.90**	6.89±8.58	8.17±10.2	**1.3 (0.6-2.0)**
	Chl (µg/l)**	G	0.15	**0.74**	0.15±0.17	0.14±0.16	0.005
FloSEE	Temperature (°C)	H	2.2	**0.97**	17.6±7.82	17.8±6.78	**0.25 (0.15-0.36)**
	Salinity (psu)	I	0.38	**0.75**	35.40±0.38	35.9±0.56	**0.47 (0.45-0.49)**
Moorings	T2 Temperature (°C)***	J	1.30	**0.23**	10.30±1.20	9.72±1.05	**0.5 (0.36-0.77)**
	T3 Temperature (°C)***	K	1.40	**0.27**	9.90±1.40	9.73±1.03	**0.2 (0.07-0.35)**
	U at B2, 78m (m/sec)	L	0.08	**0.23**	0.21±0.05	0.36±0.08	**0.16 (0.14-0.19)**
	V at B2, 78m (m/sec)	M	0.20	**0.66**	1.63±0.18	1.46±0.28	**0.16 (0.15-0.17)**
	U at B2, 156m (m/sec)	N	0.08	-0.04	0.16±0.03	0.29±0.09	**0.13 (0.11-0.14)**
	V at B2, 156m (m/sec)	O	0.18	**0.20**	1.17±0.14	1.05±0.14	**0.12 (0.10-0.14)**
Transport at 27°N	Volume (10^6 m^3/sec)	P	3.3	**0.19**	30.3±1.8	31.2±3.2	**0.91 (0.67-1.15)**

***** Unsigned difference. Bold values indicate significant correlation or mean difference at $p<0.01$. The mean difference (last column) was tested with the paired student-t test.

** Excluding points with modeled chlorophyll > 0.5 µg/l.

***Limited to low-pass (cutoff at 11-day) data, unsigned.

Table 3. Statistics of high and low frequency variability at the 4 stations

	STD high freq. (<11 day)				**STD low freq. (>11 day)**				**Correlation with temperature (low/high frequency)***			
	PT-160m	PT-296m	MT-280m	MT-417m	PT-160m	PT-296m	MT-280m	MT-417m	PT-160m	PT-296m	MT-280m	MT-417m
T	0.4	0.3	0.6	0.3	1.6	1.1	1.4	0.6				
S	0.03	0.03	0.06	0.03	0.15	0.14	0.16	0.06	**0.93/ 0.80**	**>0.98**	**>0.98**	**0.94/ 0.94**
DIC	4.1	1.7	3.2	1.0	13.0	4.1	6.8	1.1	**-0.94/ -0.88**	**-0.87**/ -0.36	**-0.93/ -0.80**	**-0.76**/ -0.09
TA	2.0	1.3	2.1	0.8	9.9	4.7	5.7	1.6	**0.94/ 0.86**	**0.96/ 0.92**	**0.98/ 0.92**	**0.76/ 0.69**
Ω_{Ar}	0.03	0.01	0.03	0.01	0.13	0.08	0.09	0.08	**0.97/ 0.96**	**0.94/ 0.81**	**0.97/ 0.90**	**0.74/ 0.57**

*Bold highlights the correlation coefficient greater than 0.5.

**Acronyms: PT – Pourtales Terrace, MT – Miami Terrace.

Captions

Figure 1. a) Model domain (delineated by the boundary of the bathymetry map) and bottom bathymetry, and b) and c) zoom-in maps for Pourtalès Terrace and Miami Terrace (see blue boxes in a)), respectively. White contours lines represent 20 m, 50 m, 100 m, 200 m, 400 m, 800 m and 1500 m. Also shown are sampling stations for GOMECC2 west Florida WFL (dots) and northern Florida Straits EFL (triangles) transects, NOAA FloSEE stations over the Pourtalès Terrace (blue dots), two SNMREC mooring stations T2 (316 m) and T3 (252 m) (green dots), and two transects (black lines) and four locations (squares) for model analysis. Note that the deeper stations along the GOMECC2 WFL transect were outside of the model domain. Also Loop Current is not shown in a).

Figure 2. Temperature versus salinity, DIC, TA, and NO_3 along the GOMECC2 WFL and EFL transects: a) T-S (also plotted are data from FloSEE cruise), b) T-DIC, c) T-TA, and d) T-NO_3. Black lines in b)-d) represent the best polynomial fits for each pair for the data along the WFL transect.

Figure 3. Model and observed integrated volume transport across 27^{o}N: a) low-frequency (>11 day) and b) high-frequency (< 11 day) components.

Figure 4. Observed (left panels) and modeled (right panels) temperature (a & b), salinity (c & d), nitrate (e & f), DIC (g & h) and TA (i & j) along the GOMECC2 EFL transect, which was surveyed in July 30-31, 2012. Modeled results shown are daily averages on July 31, 2012, when

1213 sampling for most of the GOMECC2 stations except the two at the shelf edge took place. Black
1214 dots in a) indicate the sampling depths.
1215
1216 Figure 5. Model (blue lines) and observed (red lines) near bottom temperature and currents at the
1217 two moorings on the Miami Terrace: a) near bottom temperature at T3, b) near bottom
1218 temperature at T2, c) N-S velocity (78 m) at T2, d) W-E velocity (78 m) at T2, e) near bottom
1219 (17 mab) N-S velocity at T2, and f) near bottom (17 mab) W-E velocity T2. Bold solid lines are
1220 low-pass filtered with a Lanczos filter (11-day cut-off). For observed velocities, tidal signals
1221 were removed.
1222
1223 Figure 6. A Taylor diagram for model-data correlation, root mean square of errors (RMSE), and
1224 normalized standard deviation. A is the reference point for a perfect match between model and
1225 data and the rest of the letters are corresponding to the measurements listed in Table 2. All of the
1226 modeled standard deviations (stds) are normalized by the observed stds of the corresponding
1227 variables.
1228
1229 Figure 7. Left panels: Model bottom temperature (color) and 150 m currents (vectors) over
1230 Pourtalès Terrace. Red line indicates the N-S transect across the terrace. Blue dots indicate the
1231 two locations on the platform (160 m) and over the upper slope (296 m) of the terrace. White
1232 contours indicate the isobaths of 200 m, 400 m, 600 m, and 800 m. Right panels: Model
1233 temperature (color) and W-E velocity (while contour, interval=0.2 m/sec) along the 81^{o}W
1234 transect across the Pourtalès Terrace. Red line indicates the T=12^{o}C isotherm. Note the different
1235 color scales for temperature in left and right panels.

1236

1237 Figure 8. Left panels: Model 300m temperature (color) and currents (vectors) over the Miami
1238 Terrace. Red line indicates the cross-slope (W-E) transect (~25°25'N). White contours indicate
1239 the isobaths of 200 m, 400 m, 600 m, and 800 m. Blue dots indicate the two locations on the
1240 platform (280 m) and over the upper slope (417 m) of the terrace. Right panels: Model
1241 temperature (color) and N-S velocity (white contour, >0.6 m/sec only, interval=0.2 m/sec) along
1242 the cross-slope transect. Red line indicates the T=12°C isotherm. Note the different color scales
1243 for temperature in left and right panels.

1244

1245 Figure 9. Same as Figure 8 except for bottom temperature (color) and currents (vectors) for left
1246 panels and the 25°40'N transect for the right panels.

1247

1248 Figure 10. Same as Figure 7 but for bottom DIC concentration (left panels) and DIC (color) and
1249 W-E velocity (white contour) along the N-S transect (right panels). On the left panels, the red
1250 line indicates the N-S transect, and white contours indicate the isobars of 200 m, 400 m, 600 m,
1251 and 800 m. On the right panels, the red line indicates the T=12°C isotherm. Note the different
1252 color scales for temperature in left and right panels.

1253

1254 Figure 11. Same as Figure 8 but for model bottom DIC (left panels) and DIC (color) and N-S
1255 velocity (white contour) along the W-E transect (right panels). On the left panels, white contours
1256 indicate the isobars of 200 m, 400 m, 600 m, and 800 m, and the red line indicate the W-E
1257 transect. On the right panels, the red line indicates the T=12°C isotherm. Note the different color
1258 scales for temperature in left and right panels.

1259

1260 Figure 12. Model bottom temperature (a), salinity (b), DIC (c), TA (d), and aragonite saturation
1261 state (e) at the four chosen sites on Pourtalès and Miami Terraces (see Figure 1 for locations) in
1262 2012.

1263

1264 Figure 13. (top) Annual mean distribution of bottom Omega for 2012 and (bottom) the standard
1265 deviation of bottom Omega. Depth contours (black lines) are 20 m, 100 m, 200 m, 400 m, 800 m,
1266 and 1500 m.

1267

1268 Figure 14. Temperature versus a) salinity, b) DIC, and c) TA along GOMECC2 WFL and EFL
1269 transects, at the four chosen sites on the Pourtalès and Miami Terraces (see Figure 1 for
1270 locations). Also shown are data from a subset of the WOCE A20 transect.

1271

1272 Figure 15. Modeled time-series of relative vorticity (ς) and near bottom temperature in 2012 for
1273 two sites on Pourtalès Terrace (296 m) and Miami Terrace (417 m): (a) ς at 150m and (c) bottom
1274 temperature on Pourtalès Terrace, (e) ς at 350 m and (g) bottom temperature on Miami Terrace.
1275 Their respective ς -T correlations for low-passed time-series (b and f) and anomalies (d, h) are
1276 shown on the right panels. Red lines on the right panels are the linear best fits for each pair.

1277

1278

1279

1280

1281 Figure 1.

1282
1283

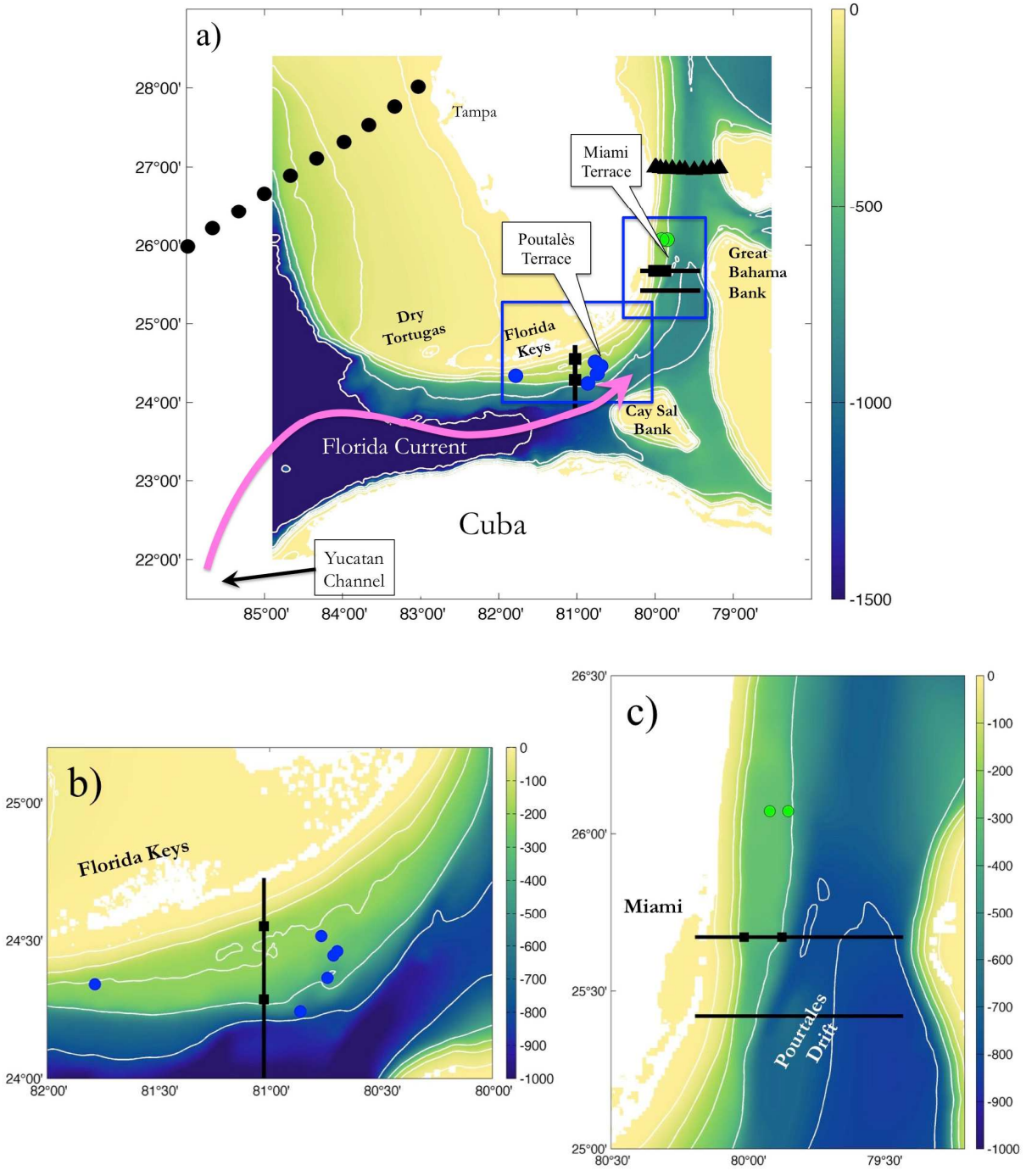

1284
1285
1286
1287
1288

1289 Figure 2.

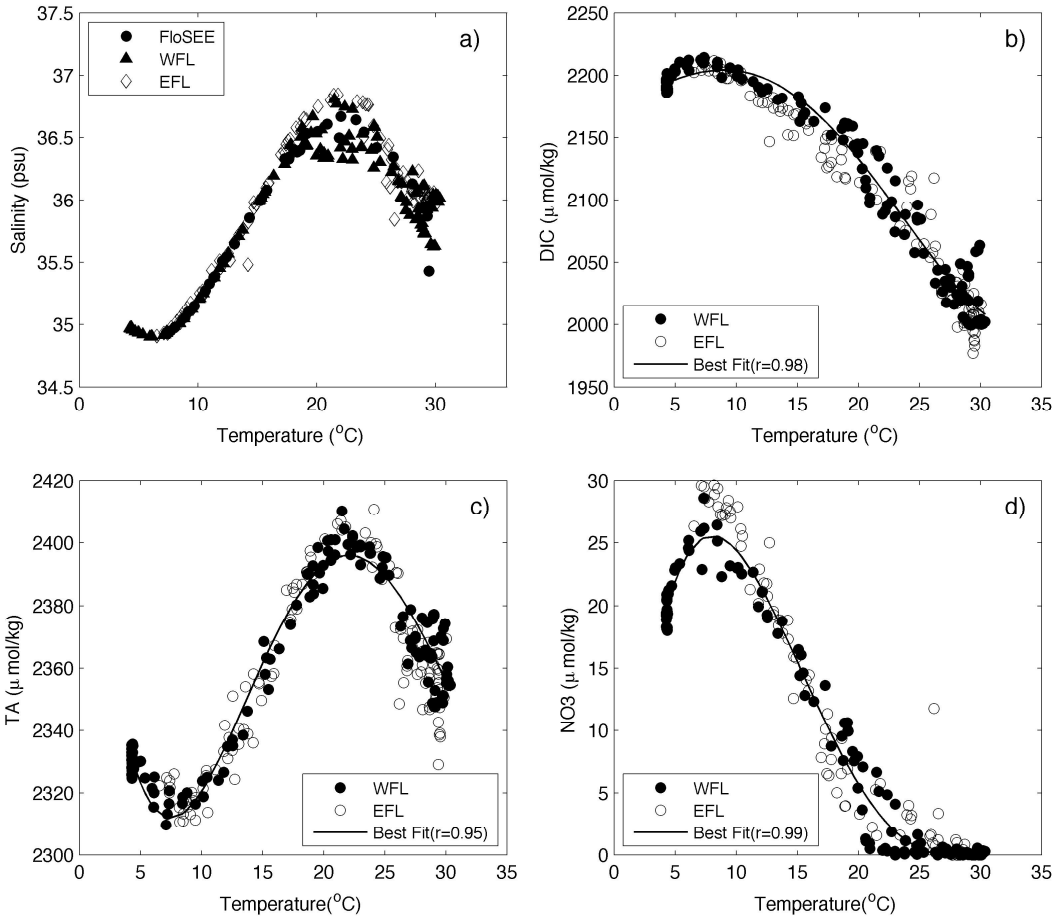

1305 Figure 3.
1306
1307
1308
1309
1310
1311
1312
1313

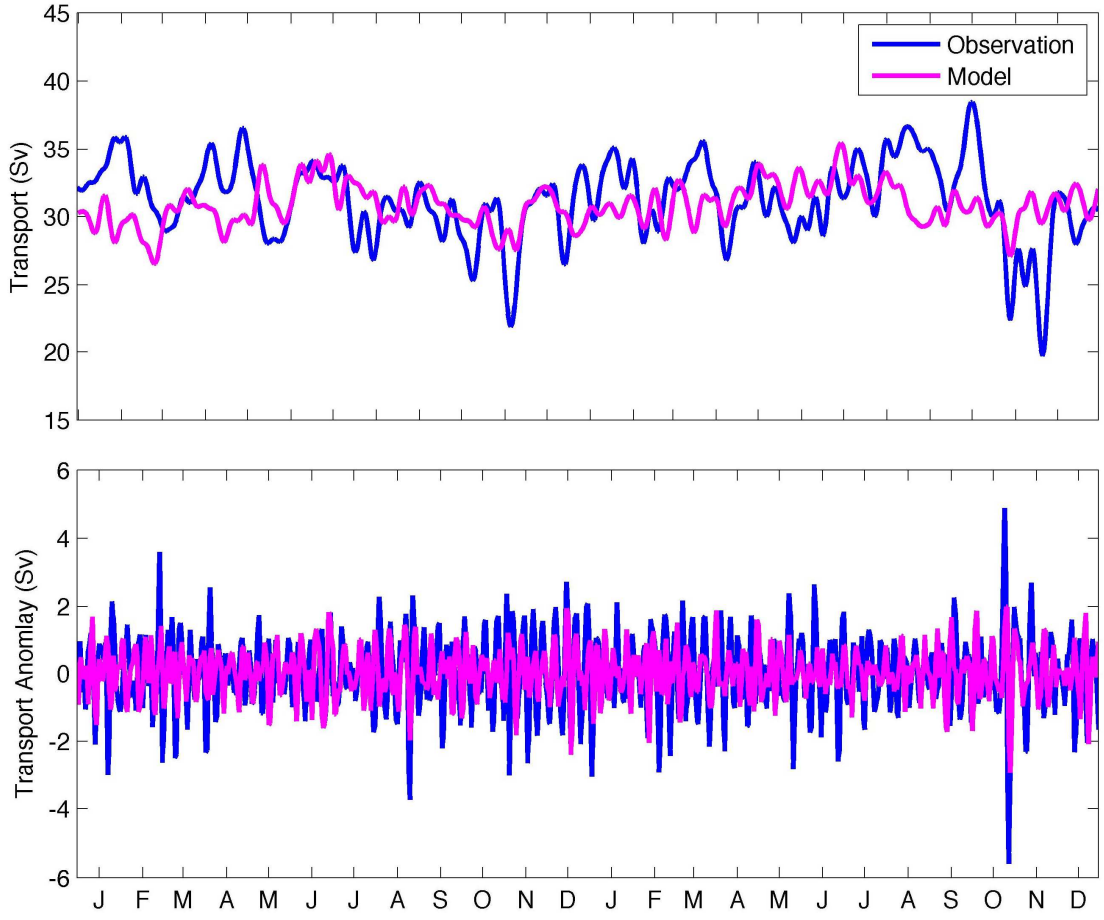

1314

1315 Figure 4.
1316
1317

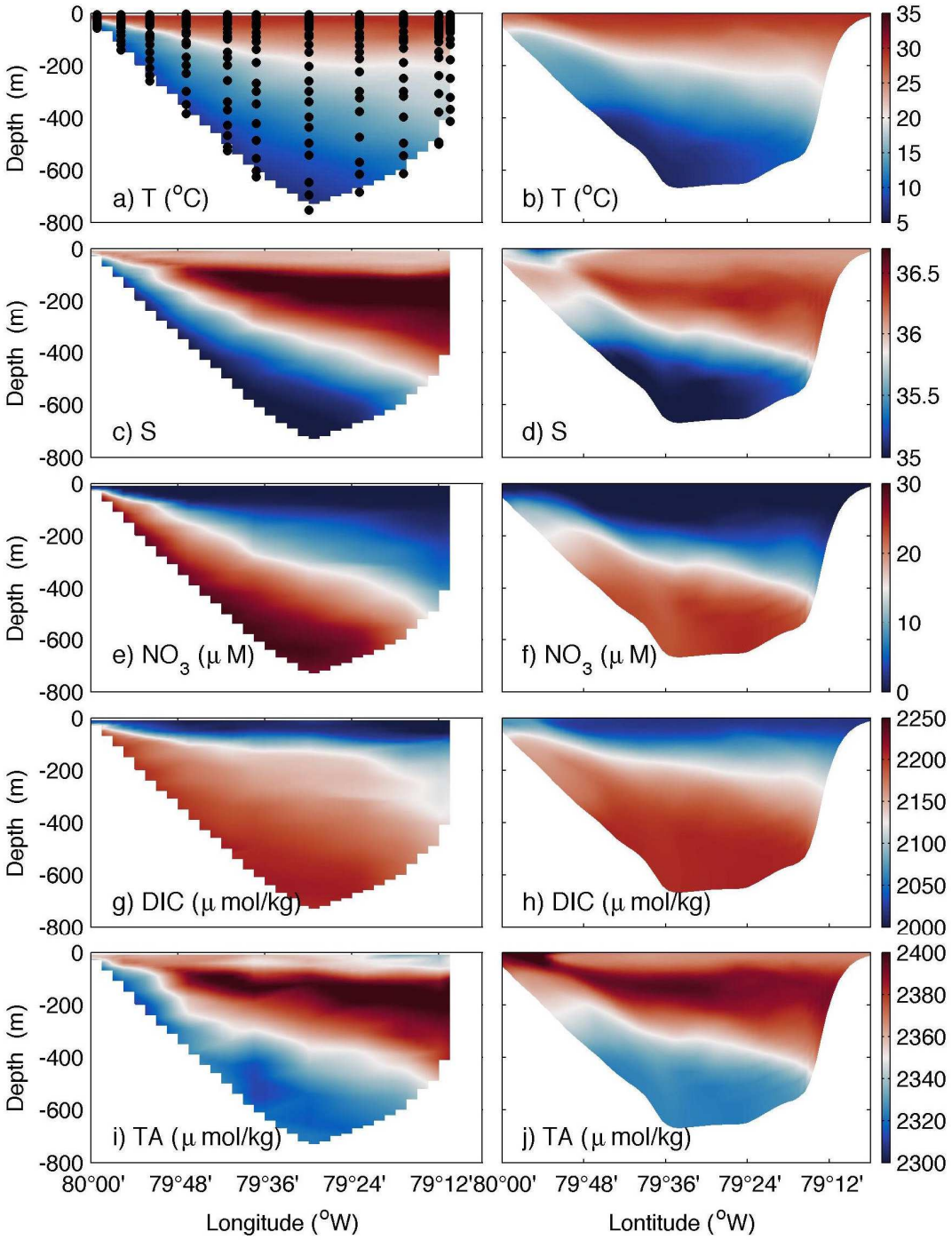

1318
1319
1320
1321

1322 Figure 5.
1323
1324
1325
1326

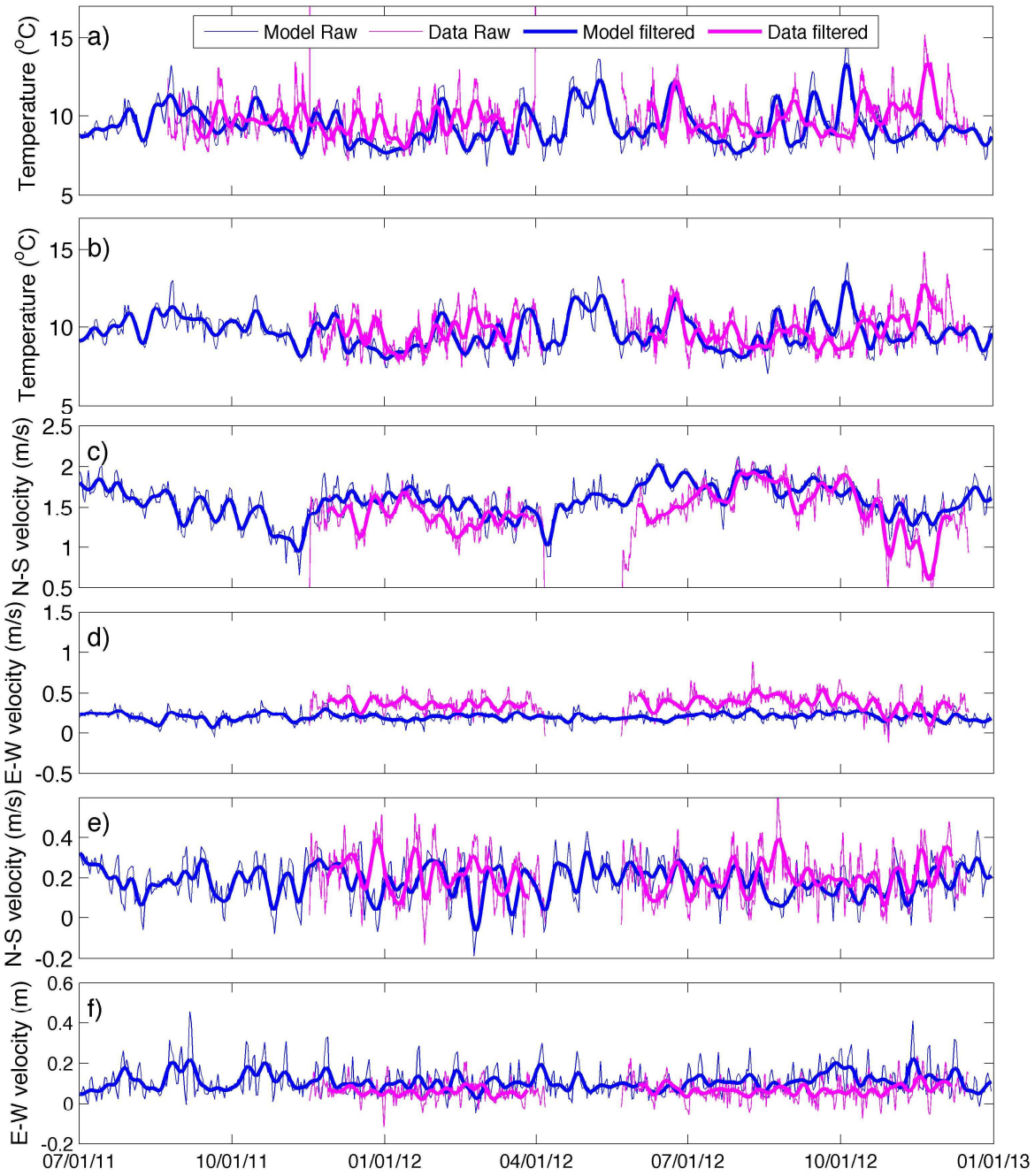

1327
1328
1329
1330

Figure 6.

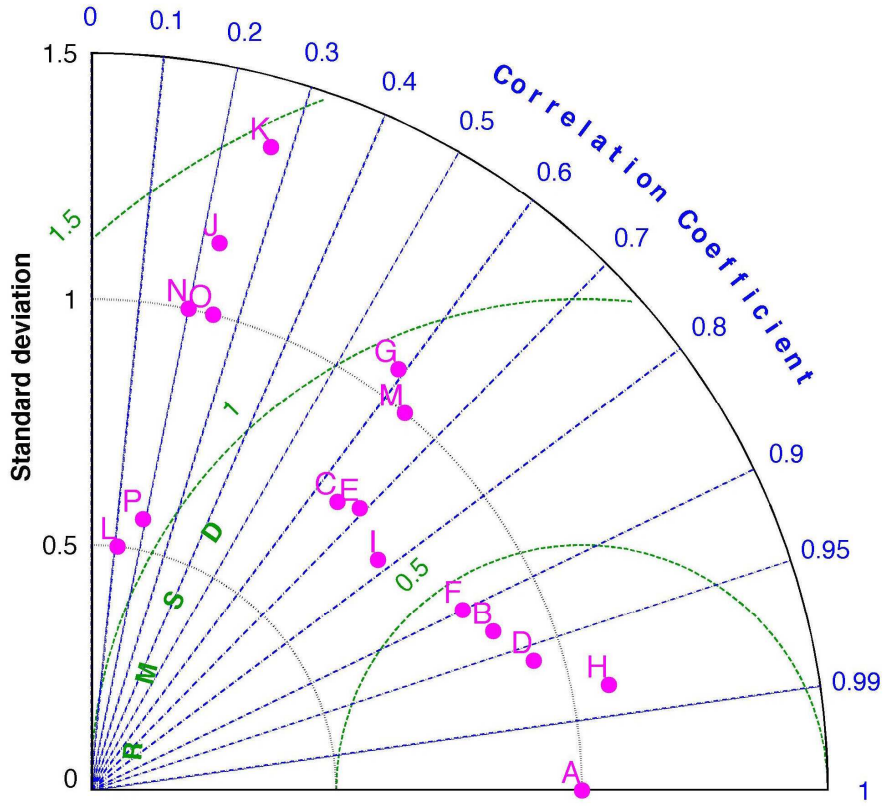
Correlation Coefficient
Standard deviation
0
0.1
0.2
0.3
0.4
0.5
0.6
0.7
0.8
0.9
0.95
0.99
1
1.5
1
0.5
0
K
J
N
O
G
M
P
L
C
F
I
F
B
D
H
A
R
M
S
D

Figure 7.

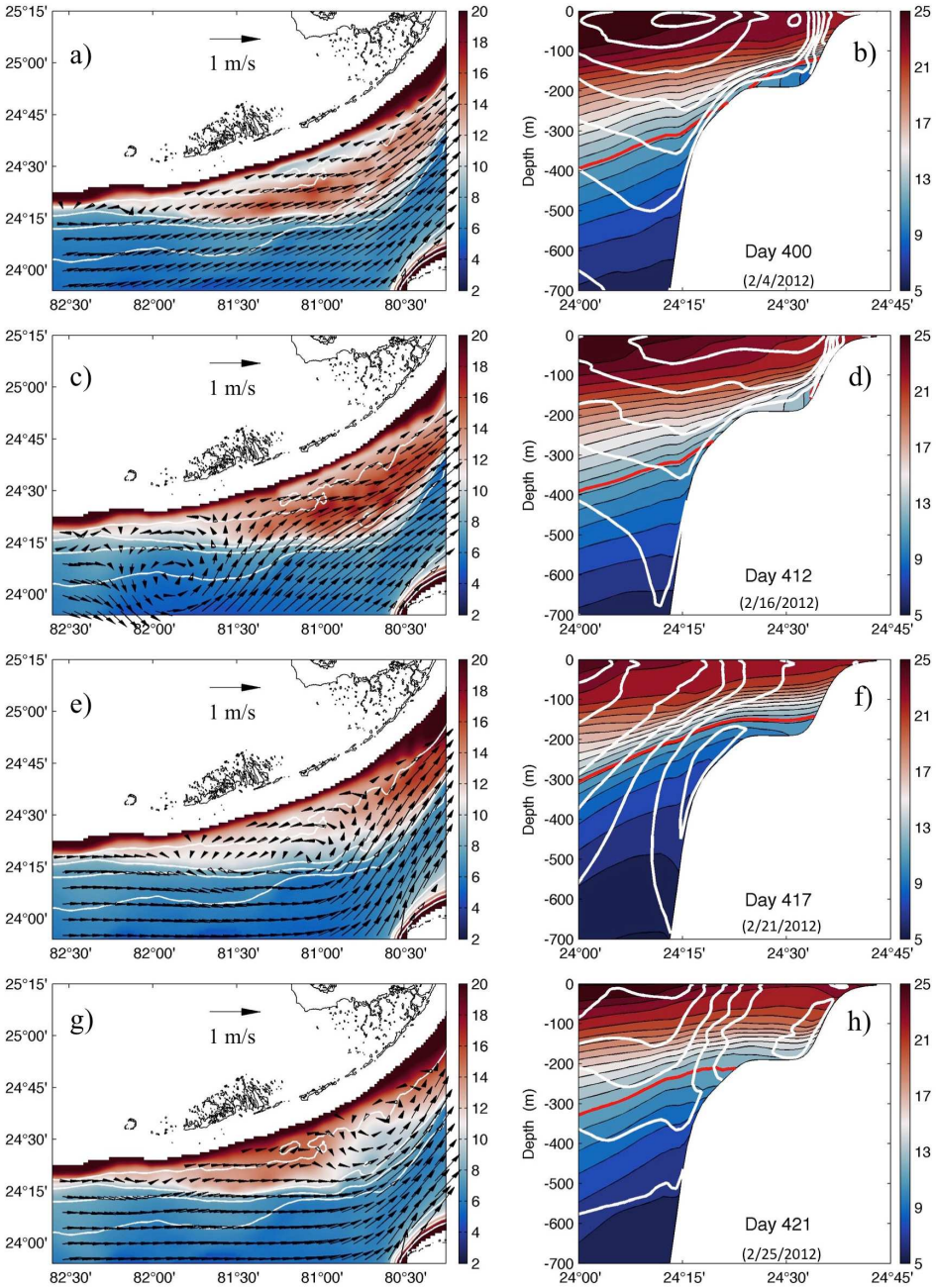
a)
1 m/s
b)
Day 400
(2/4/2012)
c)
1 m/s
d)
Day 412
(2/16/2012)
e)
1 m/s
f)
Day 417
(2/21/2012)
g)
1 m/s
h)
Day 421
(2/25/2012)
Depth (m)
25°15'
25°00'
24°45'
24°30'
24°15'
24°00'
82°30'
82°00'
81°30'
81°00'
80°30'
24°00'
24°15'
24°30'
24°45'

1355 Figure 8.
1356
1357

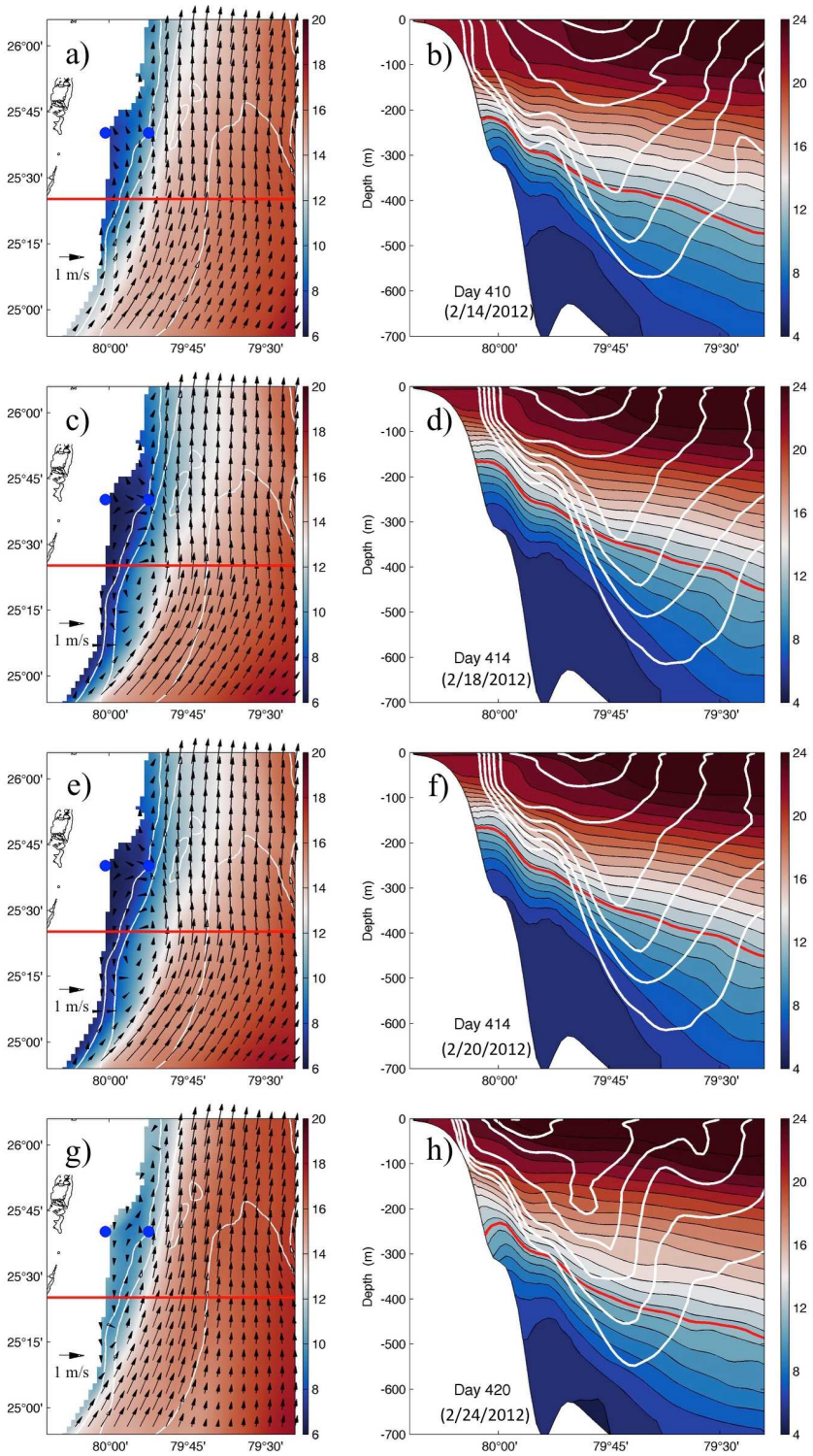

1358
1359

Figure 9.

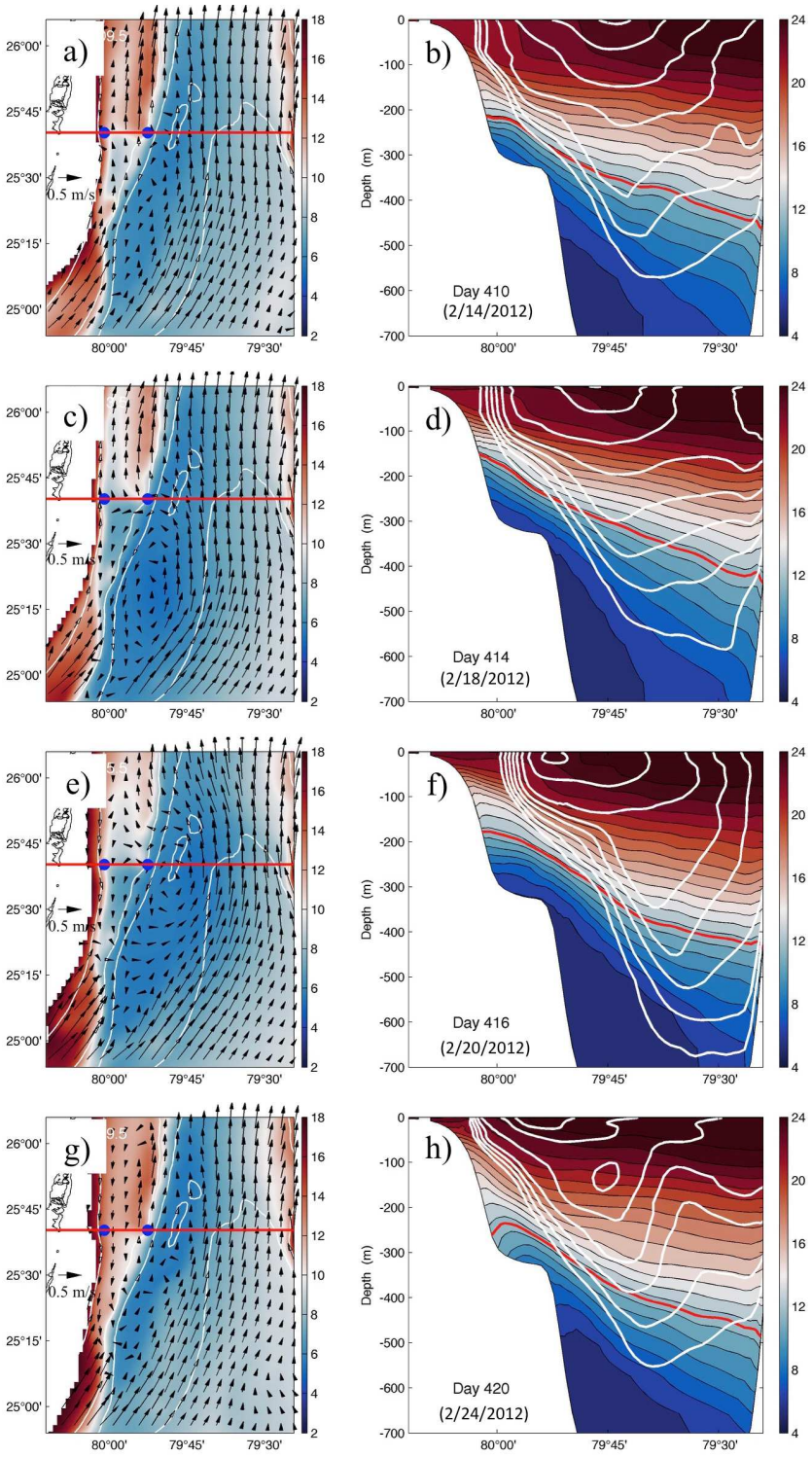
a)
b)
c)
d)
e)
f)
g)
h)
0.5 m/s
Day 410
(2/14/2012)
Day 414
(2/18/2012)
Day 416
(2/20/2012)
Day 420
(2/24/2012)
Depth (m)
26°00'
25°45'
25°30'
25°15'
25°00'
80°00'
79°45'
79°30'

Figure 10.

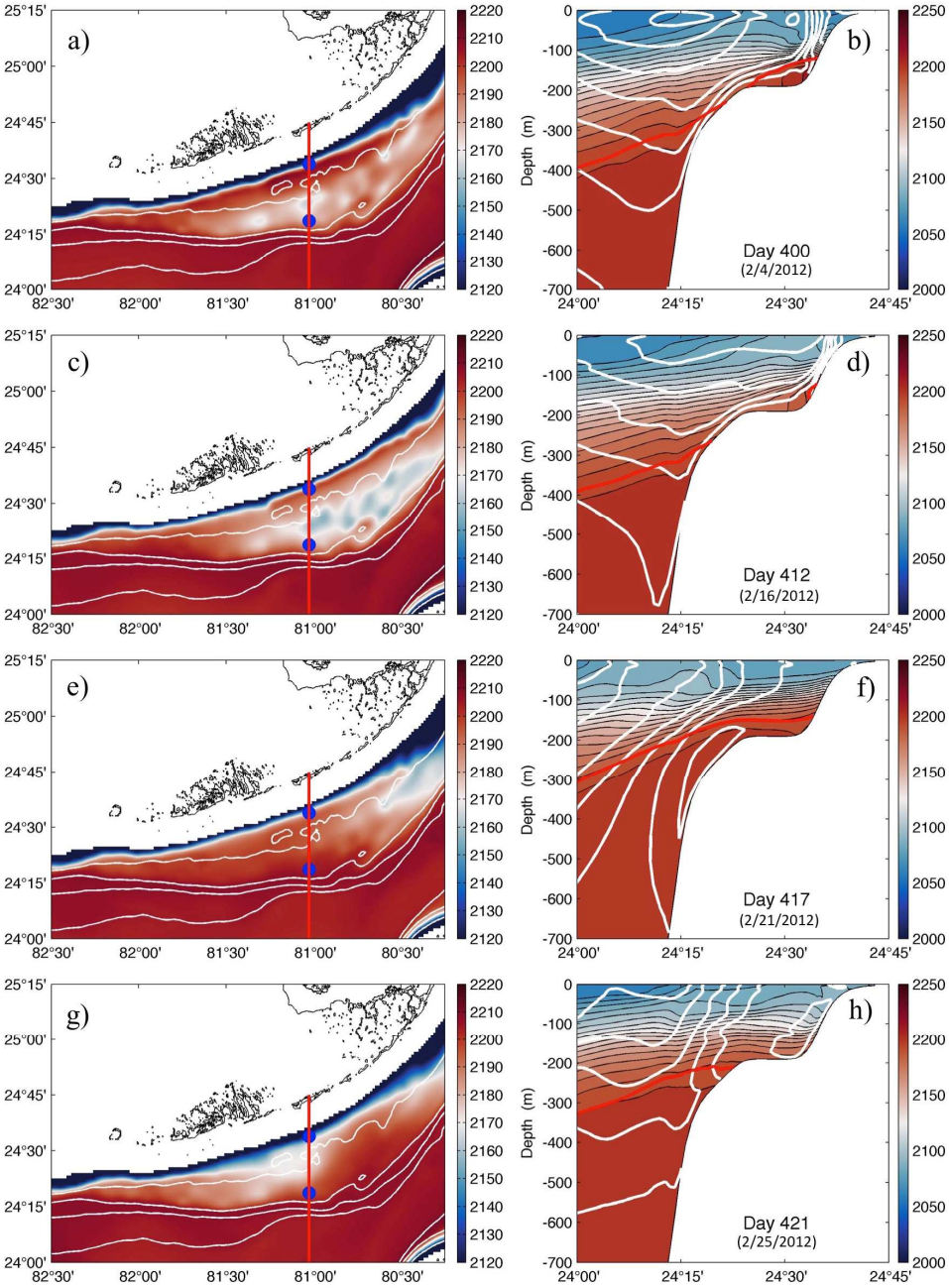
a)
b)
c)
d)
e)
f)
g)
h)
Day 400
(2/4/2012)
Day 412
(2/16/2012)
Day 417
(2/21/2012)
Day 421
(2/25/2012)
Depth (m)
25°15'
25°00'
24°45'
24°30'
24°15'
24°00'
82°30'
82°00'
81°30'
81°00'
80°30'
24°00'
24°15'
24°30'
24°45'
0
-100
-200
-300
-400
-500
-600
-700
2220
2210
2200
2190
2180
2170
2160
2150
2140
2130
2120
2250
2200
2150
2100
2050
2000

1376 Figure 11.
1377
1378

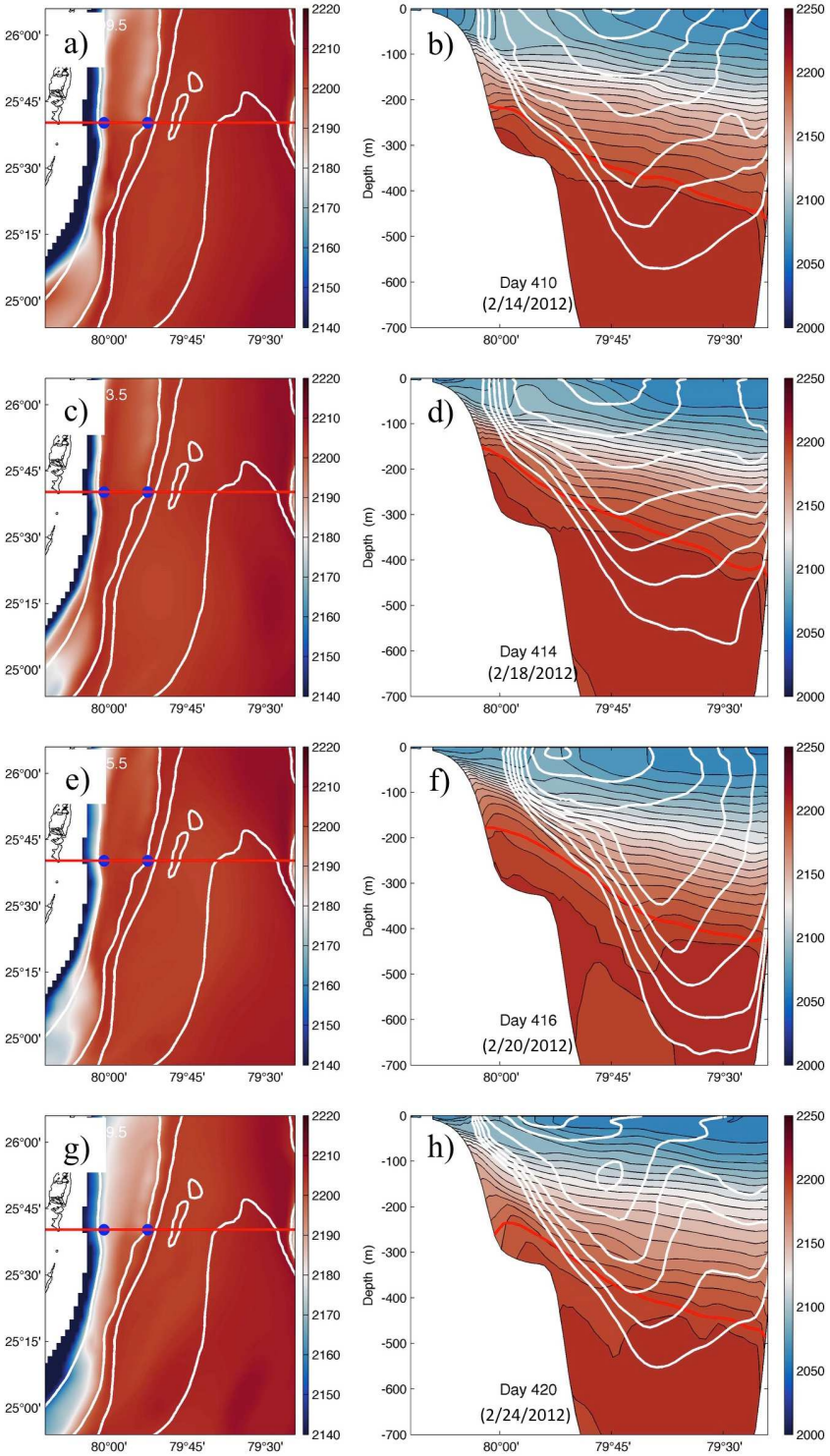

1379
1380

1381 Figure 12.
1382
1383
1384

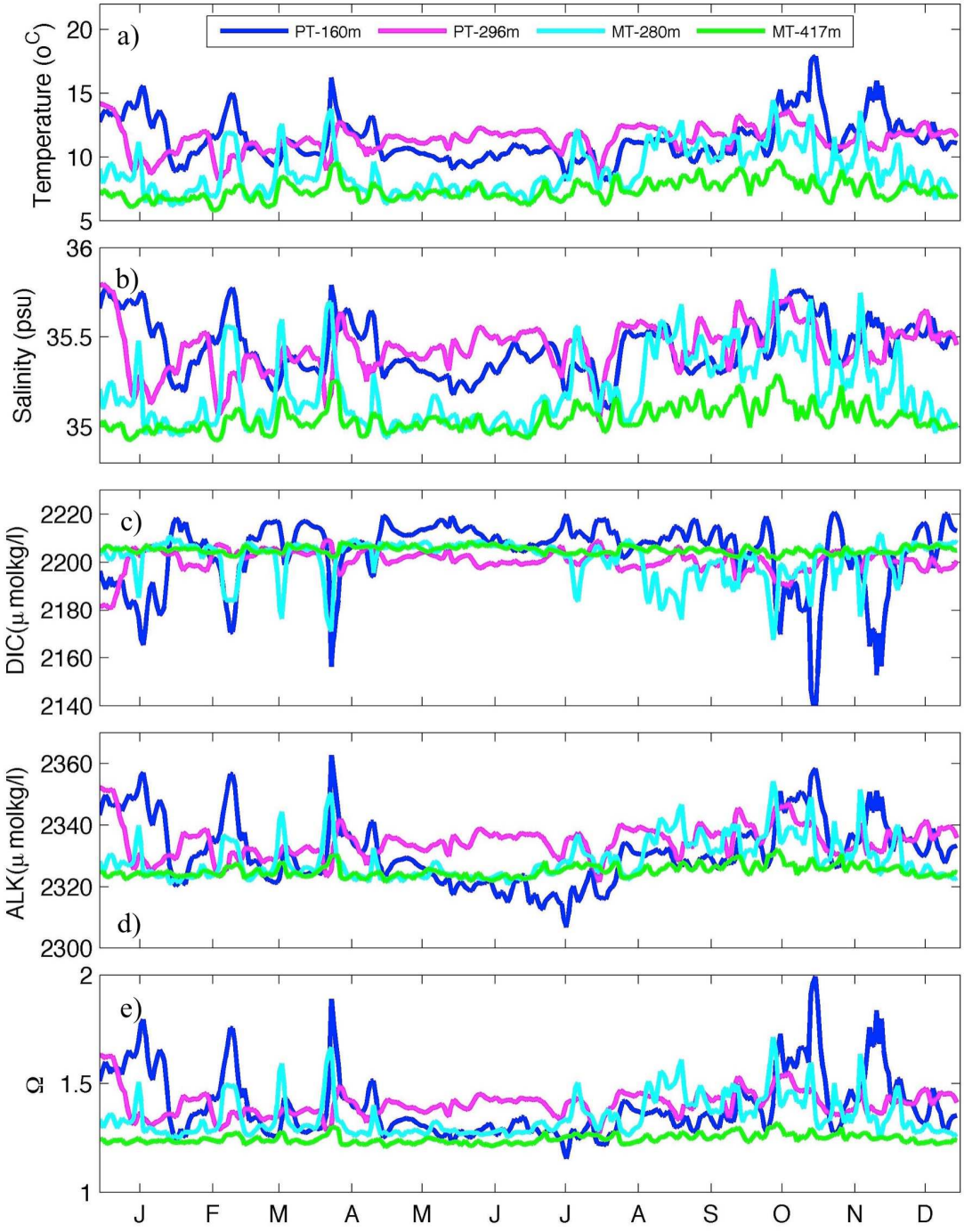

1385
1386
1387

Figure 13.

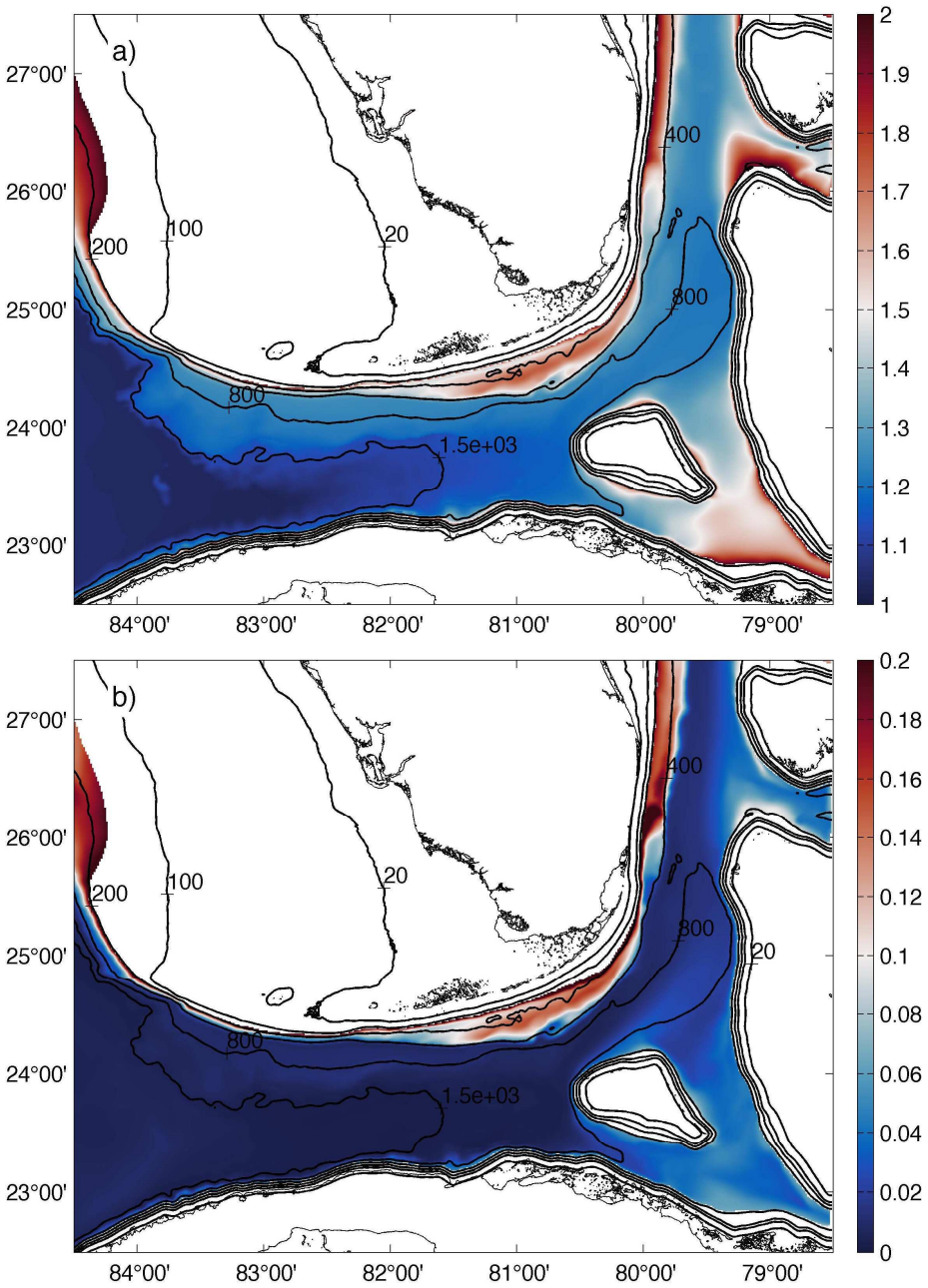
a)
b)
27°00'
26°00'
25°00'
24°00'
23°00'
84°00'
83°00'
82°00'
81°00'
80°00'
79°00'
100
200
20
400
800
1.5e+03
2
1.9
1.8
1.7
1.6
1.5
1.4
1.3
1.2
1.1
1
0.2
0.18
0.16
0.14
0.12
0.1
0.08
0.06
0.04
0.02
0

1398 Figure 14.
1399

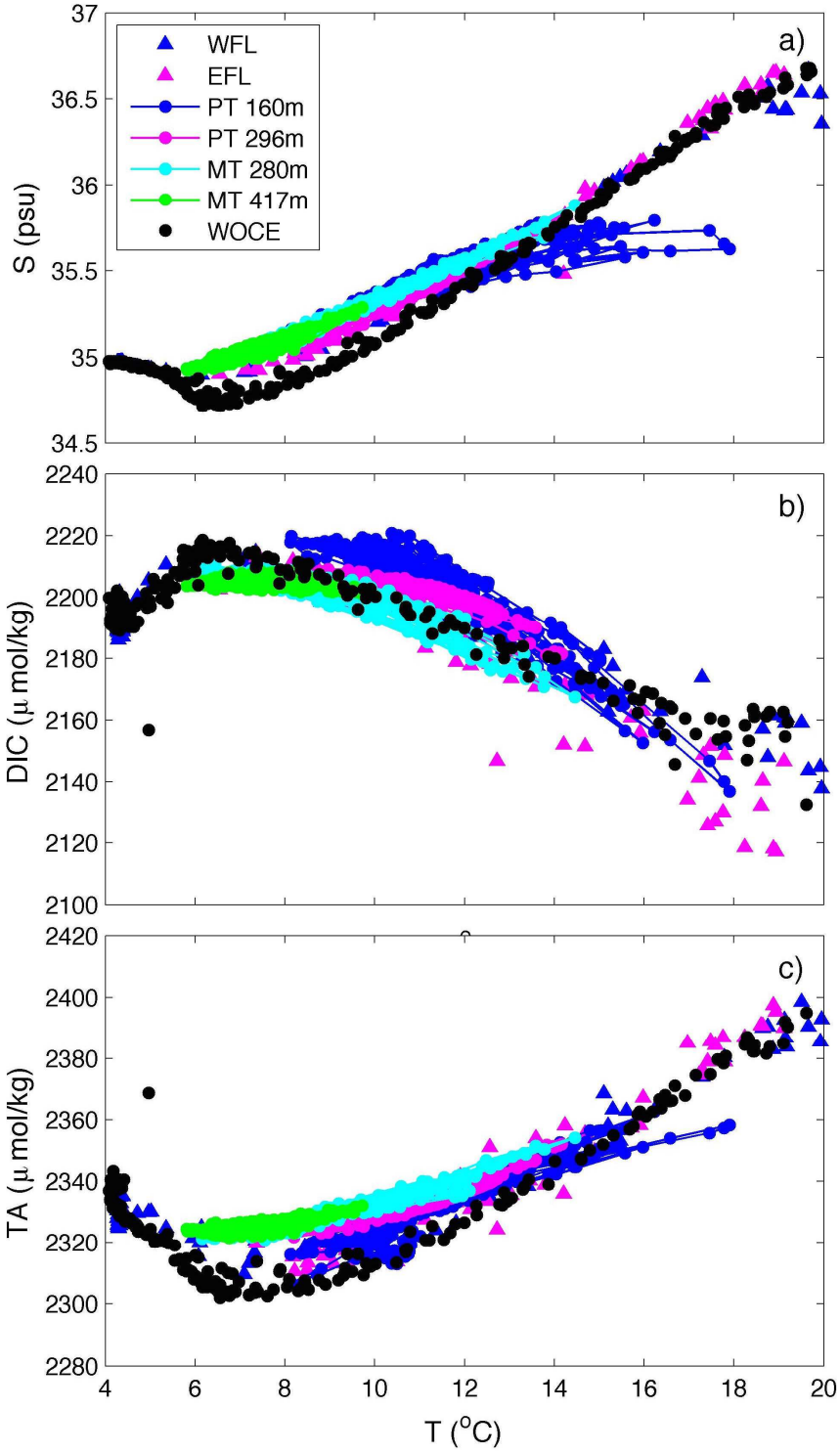

1400
1401
1402
1403

Figure 15.

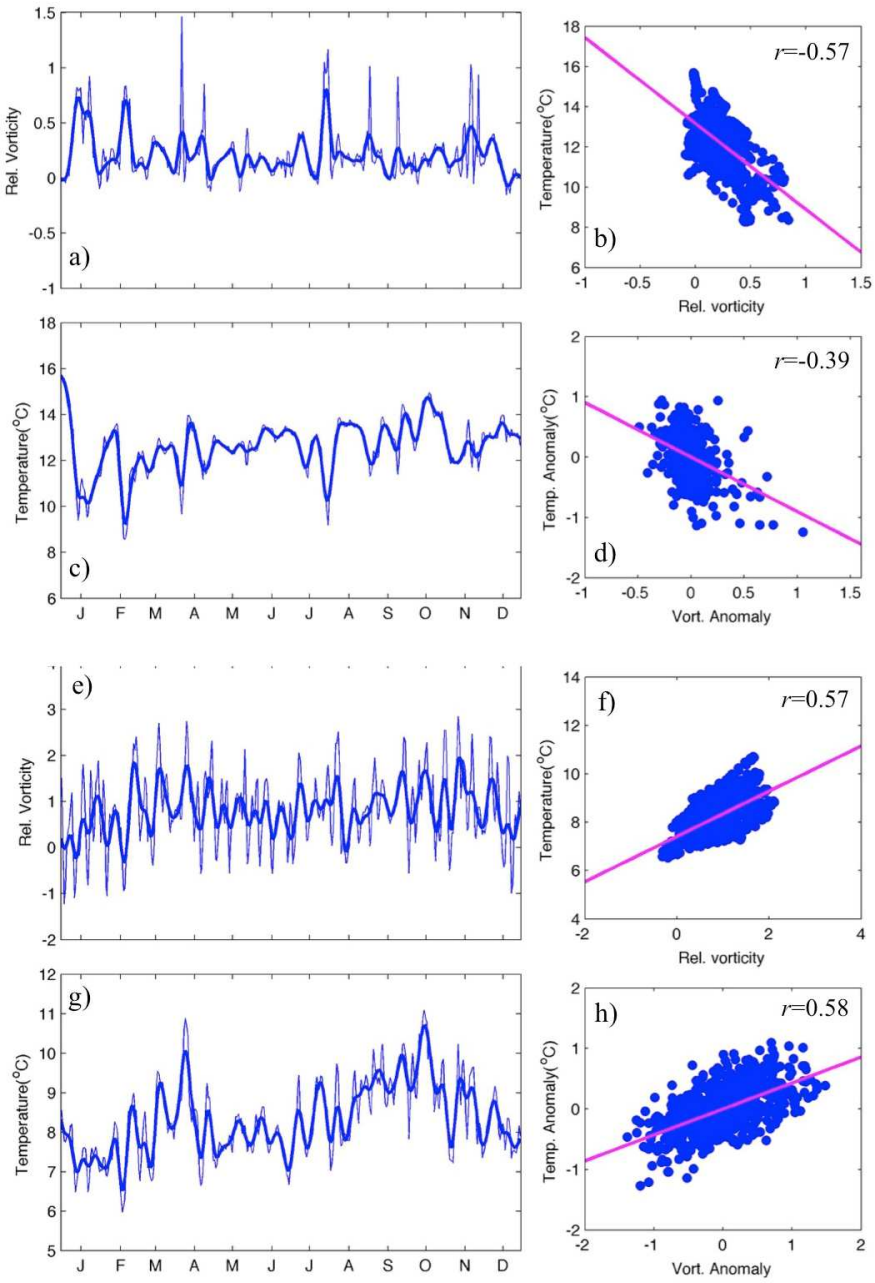
a)
Rel. Vorticity
b)
Temperature(°C)
Rel. vorticity
r=-0.57
c)
Temperature(°C)
J F M A M J J A S O N D
d)
Temp. Anomaly(°C)
Vort. Anomaly
r=-0.39
e)
Rel. Vorticity
f)
Temperature(°C)
Rel. vorticity
r=0.57
g)
Temperature(°C)
J F M A M J J A S O N D
h)
Temp. Anomaly(°C)
Vort. Anomaly
r=0.58